A New Superalloy Enabling Heavy Duty Gas Turbine Wheels for Improved Combined Cycle Efficiency

Final Technical Report

Award DEFE0026299

Prepared for
National Energy Technology Laboratory

For the Period
September 14, 2015 to October 25, 2016

Submitted by
Richard DiDomizio, Principal Investigator

Authors
Andrew Detor (GE Global Research)
Richard DiDomizio (GE Global Research)
Don McAllister (Ohio State University)
Erica Sampson (GE Global Research)
Rongpei Shi (Ohio State University)
Ning Zhou (GE Global Research)

GE Global Research
Ohio State University

This material is based upon work supported by the Department of Energy under Award Number DEFE0026299.

Table of Contents

Acknowledgement iii
Abstract iv
Table of Figures v
Table of Tables viii
1.0 Summary 1
2.0 Introduction 3
3.0 Methods 5
3.1 Characterization 5
3.2 Coprecipitation Processing 5
3.3 Oxide Dispersions Strengthening Processing 5
3.4 Mechanical Testing 6
4.0 Results and Discussion 7
4.1 Coprecipitation 7
4.1.1 Experimental 7
4.1.2 Modeling 14
4.2 Oxide Dispersion Strengthening 21
4.3 Mechanical Testing 31
4.3.1 Tensile 31
4.3.2 Hold Time Fatigue Crack Growth 33
5.0 Conclusions and Recommendations 35

Acknowledgement

The authors would like to acknowledge the technical contributions of the following people who played an integral part in producing the technical results produced on this program.

GE Global Research

Tom Bigelow, Steve Buresh, Marija Drobnjak, Brian Ellis, Jeremiah Faulkner, Mohammed Haouaoui, Chris McLasky, Nick McLasky, Scott Oppenheimer, Orrie Riccobono, Ray Roptizky, Ray Schnoor, Reza Sharghi-Moshtaghin

Ohio State University

Mike Mills, Yunzhi Wang

Abstract

The drive to increase combined cycle turbine efficiency from 62% to 65% for the next-generation advanced cycle requires a new heavy duty gas turbine wheel material capable of operating at 1200°F and above. Current wheel materials are limited by the stability of their major strengthening phase (gamma double prime), which coarsens at temperatures approaching 1200°F, resulting in a substantial reduction in strength. More advanced gamma prime superalloys, such as those used in jet engine turbine disks, are also not suitable due to size constraints; the gamma prime phase overages during the slow cooling rates inherent in processing thick-section turbine wheels. The current program addresses this need by screening two new alloy design concepts. The first concept exploits a gamma prime/gamma double prime coprecipitation reaction. Through manipulation of alloy chemistry, coprecipitation is controlled such that gamma double prime is used only to slow the growth of gamma prime during slow cooling, preventing over-aging, and allowing for subsequent heat treatment to maximize strength. In parallel, phase field modeling provides fundamental understanding of the coprecipitation reaction. The second concept uses oxide dispersion strengthening to improve on two existing alloys that exhibit excellent hold time fatigue crack growth resistance, but have insufficient strength to be considered for gas turbine wheels. Mechanical milling forces the dissolution of starting oxide powders into a metal matrix allowing for solid state precipitation of new, nanometer scale oxides that are effective at dispersion strengthening.

List of Figures

Figure 1	Typical examples showing a range of undesirable (-4 rank) to desirable (-1 rank) precipitate microstructures produced following homogenization and slow cooling.	9
Figure 2	Microstructure rank plots for experiments in 718 and R88 based alloys (see Fig. 1 for rank key). Higher values tend to produce more desirable microstructures for the current program, i.e. fine γ' or γ'/γ" coprecipitates on slow cooling.	9
Figure 3	TEM images, SAD patterns, and EDS composition maps for alloys 718-011 and 718-027 showing fine γ' and γ'/γ" coprecipitates, respectively, following homogenization and slow cooling.	11
Figure 4	Typical microstructures of modified 718 alloys following slow cooling from homogenization where the (Ti+Al)/Nb has been incrementally raised to promote γ' formation (viewed on a <011> zone axis).	12
Figure 5	Multi-axis forging sequence used to billetize and pancake 718 and modified alloys 718-011 and 718-027 in preparation for heat treatment and mechanical property testing. Optical microscopy images confirm that this process successfully breaks down the as-cast ingot into a uniform, equiaxed, fine grained microstructure.	13
Figure 6	Optical images showing the grain structure in as-forged and solution treated samples of baseline 718 and alloys 718-11 and 718-27. Three different solution heat treatment temperatures were examined all at a fixed time of 3hr: 1700˚F, 1800˚F, and 1900˚F.	14
Figure 7	Relative hardness of baseline 718 and modified 718-11 and 718-27 alloys in the as-homogenized condition and after 8 hrs aging at 1300˚F, 1400˚F, and 1500˚F with three different cooling rates (water quench and rotor rim and bore simulative).	15
Figure 8	Equilibrium shapes for composite γ'/γ'' coprecipitates with different configurations using the energy combination of $\sigma_{\gamma'} = 50.5$, $\sigma_{\gamma''} = 101$ and $\sigma_{\gamma''/\gamma'} = 75.5$ $(\mathrm{mJ/m^2})$. (a) Single lobe, (b) Sandwich, (c) Compact. The first row shows the composite particles in three-dimensions and the second row shows two-dimensional cross-sections along the yz plane through the center of the simulation box.	17
Figure 9	Analysis of atomic flux of Al during growth of γ' (red) and γ'' (dark green) particles in the sandwich and compact co-precipitates. Flux vectors are plotted as blue cones in three-dimension in the direction of the flux vector as represented by the streamline in light green. The cones have their lengths proportional to the magnitudes of the flux vectors. In (a)-(b) γ' is in contact with γ'' while in (a′)-(b′) they are separated.	18
Figure 10	Expected phase fraction of γ′ and γ″ during a heat treatment at 791°C based on precipitation modeling. The [001] diffraction patterns for samples (a) 30	19

min 791°C and (b) 60 min @ 791°C showing diffraction spots from γ′ in (a) and both γ′ and γ″ in (b).

Figure 11 SEM images of unincorporated dopants visible in both Alloy 1 and Alloy 2 due to insufficient milling energetics. This could be detrimental to properties. 22

Figure 12 SEM images of Alloy 1 showing contamination from unincorporated dopants during milling. The quantity of contamination did decrease with increasing milling energetics. 23

Figure 13 TEM images of samples N10 and N12 showing the increase in size and decrease in number density of the nanometer sized oxides (nano-oxides) with the inclusion of "z" in Alloy 1. 24

Figure 14 TEM analysis showing the increase in nano-oxide precipitation when increasing both the "x" and "y" levels with milling parameters F for time 1. 24

Figure 15 (a) Bright field TEM image and (b) EDS map showing the Al-"x" containing NFs and the γ' formed in Alloy 2 with 1x oxide loading. 25

Figure 16 Bright field TEM image and EDS maps showing that the addition of metallic dopant "z" leads to "z"-"x" rich NFs with no Al association in Alloy 2. 26

Figure 17 SEM images of Alloy 2 containing 2x "x" (N20) showing the change in microstructure and γ' distribution when the HIP temperature is increased from (a) sub-solvus HIP to (b) super-solvus HIP. 27

Figure 18 TEM images depicting the coarsening of the nano-oxides at higher HIP temperatures in both Alloy 1 (N10) "y"-based nano-oxides and the Alloy 2 (N22) "z"-based nano-oxides. 28

Figure 19 SEM images of Alloy 1 depicting the change in microstructure of due to forging. In the ODS alloys, forging increased the fine grain size as compared to the HIP microstructure. 29

Figure 20 SEM of Alloy 2 ODS (N22) depicting the increase in grain size and decrease in γ' size due to super-solvus processing. 30

Figure 21 SEM images showing Alloy 2 powder with 2x oxide and 1z metallic dopant contents in the as-forged state and after three subsequent heat treatments (T1<T3<T6<T8). The grain size increases with increases annealing temperature and the γ' solvus was found to be between T3 and T6. 30

Figure 22 Bore simulative tensile results showing a) 0.2% yield strength b) ultimate tensile strength c) plastic elongation to fail. 32

Figure 23 0.2% yield stress as a function of temperature for the 718 variants. 32

Figure 24 Hold time fatigue crack growth results for a) ODS baseline and variants and b) coprecipitation baseline and variants. 33

List of Tables

Table 1	Composition of all alloys for the coprecipitation task.	8
Table 2	Milling details for Alloy 1 milled with Praxair powder & Alloy 2 milled with CarTech Powder.	21
Table 3	Chemistry modifications evaluated for Alloy 1 and Alloy 2.	23
Table 4	Hardness results from hold time fatigue crack growth test bars.	34

1.0 Summary

The two approaches screened on this program to enable a 1200°F capable heavy-duty gas turbine wheel were the coprecipitation of γ'/γ'' and oxide dispersion strengthening. The primary screening method for each of these approaches was a microstructure evaluation following a conservatively slow cooling rate that mimics the slow cooling rate seen in thick sections of heavy-duty gas turbine wheel forgings. The most promising alloys that exhibited microstructures with fine precipitates were then fully processed to allow mechanical test specimens to be machined and tested. The mechanical tests screened were tensile properties to evaluate turbine wheel bore behavior and hold time fatigue crack growth to evaluate rim behavior.

The coprecipitation task melted and screened the microstructure of 67 alloys. The initial microstructure screening following a conservative slow cool resulted in three types of alloys:

1) Alloys with precipitates that were too coarse to provide useful strengthening or had heavy topologically close packed (TCP) phase formation
2) Alloys that exhibited γ'/γ'' coprecipitation
3) Alloys that exhibited fine γ' without coprecipitation (these alloys were subsequently termed sluggish γ')

The coprecipitation and sluggish γ' alloys with the finest γ' were then billetized/forged, solutioned, and aged prior to tensile testing and hold time fatigue crack growth testing. While both alloys tested showed the necessary ductility, neither alloy was strong enough or had sufficient hold time fatigue crack growth resistance to meet design requirements. Additionally, it was found that the aging procedure used was not optimized as additional strengthening occurred during the hold time fatigue crack growth tests.

A multi-phase field model to predict γ'/γ'' coprecipitation was developed and validated over the course of the program. The model started by assuming isothermal γ'/γ'' coprecipitation to enable a parametric study of critical parameters to provide values that yielded a predicted equilibrium shape matching experimental results. Once these parameters were identified, the model was continually extended and validated until it was able to predict the heterogeneous nucleation of γ'/γ'' coprecipitates upon cooling.

The oxide dispersion strengthening task screened 29 combinations of chemistry and processing parameters. Unlike the coprecipitation task where the processing was largely fixed, mechanical milling processing parameter development on the oxide dispersion strengthening task was an integral part of achieving the desired microstructure. An initial set of processing parameters was chosen to balance microstructure and maximum yield. However, subsequent microstructure analysis showed that more aggressive milling was required to fully incorporate all elemental additions, significantly reducing yield. Three alloys were prepared for mechanical testing by HIPing, forging, and annealing/aging. The tensile results showed that the oxide dispersion strengthened alloys had strengths well in excess of what was required for design. However, the alloys had poor ductility and very poor hold time fatigue crack growth behavior.

The screening work completed demonstrates that it is technically feasible to create the intended microstructures for both concepts. Controlled γ'/γ'' coprecipitation is possible during a conservative slow cool process that simulates production thick sections and homogeneous distributions of nanometer-sized oxides are possible in both solid solution and γ' strengthened nickel superalloys. While neither method met all required screening properties, there are clear chemistry, processing, and microstructure modifications that can be made to improve the balance of properties. Moving forward, it is recommended that only the γ'/γ'' coprecipitation continues. The balance of properties of this concept is closer to meeting design requirements. Further, the extremely low process yield of the oxide dispersion task makes property screening difficult and suggests that future scale up will be extremely difficult.

2.0 Introduction

The most efficient way to generate power today is through the use of a combined cycle power plant that pairs heavy duty gas turbines with a steam turbine. In this format, GE's state-of-the-art HA turbines have a combined cycle efficiency of approximately 62%. However, to generate a step change in cycle efficiency capability of 65% or greater, significant improvements in turbine aerodynamic performance, secondary flow reduction, and combustion technology are required. Ultimately, these design improvements require higher compression ratios and higher temperatures than today's cycles. While design concepts exist to enable these cycle changes, the materials available today cannot meet the stress and temperature requirements in order to sustain the improved cycle parameters. In particular, heavy duty gas turbine wheel materials need significant advancement to enable the step change in efficiency.

The above cycle improvements work in concert to enable greater efficiency by increasing both the temperature and stress experienced by the heavy duty gas turbine wheel. Turbine aerodynamic performance can be improved by reducing turbine loading and lowering turbine thru flow. The former is achieved by increasing the flowpath radius, while the latter is achieved by increasing the flowpath annulus. These two design changes ultimately lead to larger and heavier turbine wheels which rotate at a larger effective radius. Thus, the strength capability of the heavy duty turbine wheel must increase to enable better turbine aero performance. The other two areas of technology, secondary flow and combustion, work together to raise gas path temperatures while managing overall cooling flows to maximize performance benefits. As cycle temperatures rise, the optimum pressure ratio for that cycle to operate also rises, leading to significant additional combined cycle performance benefits for higher pressure ratios. Furthermore, higher pressure ratios are required to keep exhaust temperatures manageable because plant accessories, such as the heat recovery steam generator, will become considerably more expensive and complex beyond a certain exhaust temperature threshold. Due to the higher pressure ratio and higher temperatures, heavy duty gas turbine wheel alloys with better temperature capability are required. To drive to 65% combined cycle efficiency, today's pressure ratios need to grow. In turn, this drives up the temperature experienced by the heavy duty gas turbine wheels. The heavy duty gas turbine wheel must enable this higher temperature capability while simultaneously bearing the larger stresses required for the aero improvements, which is not possible using today's available materials. Thus, a next generation heavy duty wheel material is required and it needs to operate at temperatures in excess of 1200°F. Further, the wheel material needs to operate at these higher temperatures and stresses for turbine lives on the order of 15–20 years.

Recent advances in ceramic matrix composites, intermetallic alloys (such as $MoSi_2$ and NbSi), single crystal superalloys, and coating technologies have all allowed temperature advances to occur for hot section components, including shrouds, nozzles, buckets, and combustor liners. However, similar advances in materials technology that allow step changes in temperature performance have not occurred for heavy duty gas turbine wheels. Thus, the drive to higher overall turbine efficiencies is being limited by current wheel materials technology. This program will screen two materials concepts, coprecipitation of gamma-prime (γ') and gamma-double-prime

(γ'') in a gamma (γ) matrix, and oxide dispersion strengthening (ODS) of nickel superalloys to achieve a 1200°F capable wheel material.

While the overall balance of properties must be maintained, key rim properties that must be improved at this elevated rim temperature include creep strength, low cycle fatigue, sustained peak low cycle fatigue, continuous cycle fatigue crack growth, and hold time fatigue crack growth (HTFCG). The alloy also needs to withstand tensile stresses that are present at the wheel bore. This required balance of properties restricts candidate alloys to nickel-based superalloys such as the γ''-strengthened 706 or 718 and the γ'-strengthened alloys 718Plus or R88DT. Another γ'-strengthened alloy, Haynes 282, is currently being considered for next generation steam turbine cycles at temperatures of approximately 1400°F. However, the maximum stresses experienced in a steam turbine rotor are much lower than those experienced in a gas turbine wheel. As a result, this excludes conventional Haynes 282 from consideration.

The Ni-based superalloys under consideration can be divided into three general categories depending on the strengthening phase present. Alloys such as 625 are strengthened via solid solution with some contribution from carbides, and the overall strength is typically too low to be used under the high temperatures and stresses experienced by turbomachinery wheels and disks. Alloys such as 718, 725, and 706 are strengthened primarily by γ'' and are currently used for heavy duty gas turbine wheels. Alloys such as Haynes 282, 718Plus, and R88DT are primarily strengthened by γ'. When the γ' content is high enough, this class of alloys can reach sufficient strength to be used for jet engine disks (R88DT).

Alloys strengthened with γ' are routinely used at operating temperatures in excess of 1200°F while still meeting all mechanical property requirements in jet engines; however, their processing requirements make them impractical to manufacture on the scale required for heavy duty gas turbine wheels while still retaining all necessary properties. In particular, to achieve the necessary properties in both wheel bore and rim sections, a critical rapid cooling rate is required throughout the forged part after solution heat treatment. This limit is based on prior GE design studies of critical properties as a function of cooling rate. As a result of this size difference, and the thermal inertia associated with the larger heavy duty gas turbine wheel, it is not possible to achieve the required cooling rate throughout the wheel. This results in overaged γ' leading to properties that are insufficient to meet life requirements. Alloys strengthened with γ'' have two issues preventing their use as 1200°F capable heavy duty gas turbine wheels. The first is the metastable nature of γ'', which begins to rapidly coarsen at temperatures above approximately 1150°F, resulting in a substantial drop in mechanical behavior after the prolonged exposure typical of heavy duty turbine wheels. A second issue is the poor HTFCG resistance of many γ'' alloys at temperatures of 1100°F and above when compared to solid solution strengthened or γ'-strengthened alloys.

Because of the property and thick section processing limitations of currently available steels, γ'' nickel superalloys, and γ' nickel superalloys, a clear need exists for a new 1200°F, thick section capable material to enable a 65% efficient gas turbine.

3.0 Methods

The following processes and methods were utilized on this program.

3.1 Characterization

SEM characterization was performed using a Hitachi SU70 FEG-SEM with high resolution backscattered electron (BSE) imaging using a Y-Al garnet (YAG) scintillator detector. TEM characterization was performed using a Tecni-Osiris TEM, field emission microscope operated at 200KV. This microscope is equipped with 4 Bruker SDD detectors for faster x-ray signal acquisition. It also has a STEM bright field detector which is complimentary to the STEM-HAADF detector. In order to prepare a TEM sample, a thin slice with 1mm thickness was cut using a low speed saw. It was then mechanically ground with SiC paper to 100-120μm thickness. 3mm disks were punched out from thinned slices. A Fischione1100 twin jet machine was used to electropolish the foils in 20% methanol in Perchloric acid at -50°C. After perforation the thin foils were rinsed in methanol and distilled water before being placed in the TEM.

3.2 Coprecipitation Processing

All samples were produced in a small vacuum induction melter at GE Global Research, yielding ingots of approximately 1-3/8in diameter x 3in tall. After melting, a section was cut from each ingot for homogenization heat treatment followed by slow cooling to room temperature. A slow cool was imposed to conservatively simulate conditions in the thickest section of a large gas turbine wheel as finite element analysis has shown that cooling rates can reach the single digit °F/min range for large parts undergoing static air cooling. This conservative test was used to screen alloys for the coprecipitation mechanism. Coprecipitation must occur on cooling and be capable of controlling γ' coarsening under these severe conditions. After heat treatment, alloys were prepared using conventional metallographic techniques and etched to reveal any precipitation. All samples were then examined in a scanning electron microscope (SEM). Alloys containing coarse γ' (>1μm) or significant amounts of other undesirable phases (such as the family of topologically close packed, or TCP phases) were excluded from further analysis. Select promising alloys were examined at higher magnification in a transmission electron microscope (TEM) to characterize details of the precipitating phase(s) and the occurrence of coprecipitation. Those alloys selected for mechanical testing based on the above screening were converted to a fine-grained equiaxed microstructure using multi-axis forging. After multiple reductions along the 'A', 'B', and 'C' axes, a final upset to approximately 1in thickness at a reduced strain rate was completed. The forging was then solutioned, cooled at the appropriate cooling rate, and then aged prior to being machined and tested.

3.3 Oxide Dispersion Strengthening Processing

All mechanical milling took place at GE Global Research in a Zoz CM-01 high speed attritor mill. The mill was evacuated and backfilled with Ar three times prior to starting to ensure milling occurred in an inert atmosphere. The mill charge included 150g of a pre-mixed physical mixture

of metal and oxide and 1.5kg of steel shot milling media. The mill was then run via computer control to the desired speed and time parameters. Following milling, the powder was unloaded into lab air if the powder was meant only for microstructure evaluation screening. The powder was then sieved at 30mesh to remove any large particles and the powder that passed through (the useable yield) was packed into a valved stainless steel HIP can, welded closed, leak checked, and evacuated and degassed at room temperature and elevated temperature before being crimped and welded shut. The milled powder meant for mechanical testing was unloaded directly in an Ar-filled glovebox where it was welded into a valved HIP can in the glovebox. This ensured that the milled powder was never exposed to an oxygen-rich environment when in the powder state. Once sealed after evacuation, the HIP cans were HIP'd at varying temperatures. Those alloys selected for mechanical testing were HIP'd, forged, and annealed or solutioned prior to being cooled at the appropriate rate.

3.4 Mechanical Testing

All tensile tests were conducted on blanks that had been cooled from solution or annealing temperature at a bore simulative condition. This cooling rate simulates the bore of a wheel operating at next generation turbine conditions. Threaded tensile bars were extracted perpendicularly to the forging direction. The straight section gage length was 0.5in and the gage diameter was 0.089in. Tensile tests were conducted on a closed loop servo controlled hydraulic test frame at a constant displacement rate of 0.02 in/min. The samples were heated in a resistive furnace and soaked for 15min at the test temperature prior to beginning the test. An extensometer was not used and the final reported yield strength values are corrected for machine compliance. All hold time fatigue crack growth tests were conducted at a rim simulative condition on blanks that had been cooled from solution or annealing temperature at a rim simulative rate. Compact tension samples were extracted from forgings in a C-R orientation (simulates a crack being stressed by the hoop stress of a spinning wheel). The width of the compact tension sample was 0.8in and the thickness at the base of the side grooves was 0.2236in. A pre-crack sequence starting from the end of the electro-discharge machined (EDM) notch was completed at test temperature to produce a sharp crack. The hold time crack growth tests were then run at a constant stress intensity factor range while including ever increasing hold times at the maximum stress. Crack growth control and monitoring were completed using a reversing DC electrical potential system. Experimental beachmarks were correlated with the potential drop distance measurements to ensure accuracy prior to reducing the data.

4.0 Results and Discussion

The following section summarizes the results obtained during the entire duration of the program. For more detailed descriptions of individual results and references of background research, the reader is encouraged to review the individual quarterly reports.

4.1 Controlled Coprecipitation

The goal of the controlled coprecipitation task is to use heterogeneous precipitation of gamma-double-prime (γ'') on the surface of γ' to slow coarsening kinetics on cooling.

4.1.1 Coprecipitation Experimental Results

A total of 67 alloys were melted over a one year program to explore the concepts of controlled coprecipitation and sluggish γ' to enable next generation large industrial gas turbine wheels. Table 1 lists the relative levels of Al, Ti, and Nb for all alloys on a color scale where green is low and red is high. The alloys are broadly categorized into those based on commercial R88 and IN718 compositions. These two systems were chosen to represent well understood γ' and γ'' forming alloys, respectively. The modified alloys listed in Table 1 are all attempts to understand and manipulate γ'/γ'' coarsening on slow cooling to simulate large part processing conditions, with the aim of maintaining a fine (<1μm) precipitate structure composed primarily of the stable γ' phase. Based on thermal simulations, a conservative slow cooling rate from homogenization heat treatment was chosen as a screening condition and each alloy was characterized following this exposure to identify the presence of either fine γ' or fine coprecipitates of γ'/γ''. Many alloys were excluded early due to large, undesirable γ' or TCP formation easily observed by optical microscopy or low resolution scanning electron microscopy (SEM). A small subset of alloys, however, showed promising microstructures and were subsequently examined in more detail via transmission electron microscopy (TEM). Of this subset, alloys 718-011 and 718-027 were chosen for further study due to presence of fine γ' and fine γ'/γ'' coprecipitates, respectively, following slow cooling from homogenization. Forging, solution treatment, and aging heat treat studies were then conducted on these alloys to produce material for mechanical testing. A review of key results follows and reference is made to quarterly reports for more detail as appropriate.

		Relative Composition		
Alloy Name	Notes/Purpose	Al	Ti	Nb
R88	R88 Baseline			
R88-001	R88 Base with Al-Ti-Nb Mixture DoE			
R88-002				
R88-003				
R88-004				
R88-005				
R88-006				
R88-007				
R88-008				
R88-009				
R88-010				
R88-011				
R88-012	R88 Base, Higher Nb to Promote γ"			
R88-013				
R88-014				
718	718 Baseline			
718-001	718 Base Al-Ti-Nb Mixture DoE			
718-002				
718-003				
718-004				
718-005				
718-006				
718-007				
718-008				
718-009				
718-010				
718-011				
718-012	718 Base, Higher Al/Ti to Promote γ'			
718-013				
718-014				
718-021	S-R Space DoE			
718-022				
718-023				
718-024				
718-025				
718-026				
718-027				
718-028				
718-029				
718-030				
718-031				
718-032				
718-033				
718-034				
718-035				
718-036	Alloys to Inform Precipitation Model			
718-037				
718-038				
718-039	718-11 Mod Al/Nb Ratio			
718-040				
718-041				
718-042	718-11 Mod Increase Ti			
718-043				
718-044				
718-045				
718-046	718-11 Mod Ti/Al Ratio			
718-047				
718-048				
718-049				
718-050	718-11 Mod Tie Line Study			
718-051				

Table 1: Relative Al, Ti, and Nb levels of all alloys processed and characterized on this program (green = low, red = high).

Figure 1 contains example microstructures produced following homogenization and slow cooling covering the range of structures observed for those alloys listed in Table 1. To examine broad trends, we categorize the microstructure on a scale from -4 to -1 per the follow descriptions:

-4 Large precipitates or TCP phases
-3 Fine acicular precipitates
-2 Fine dendritic precipitates
-1 Fine spherical/cuboidal precipitates

For the purposes of the present work structures on the higher end of this scale (-1) are more desirable than those at the lower end (-4).

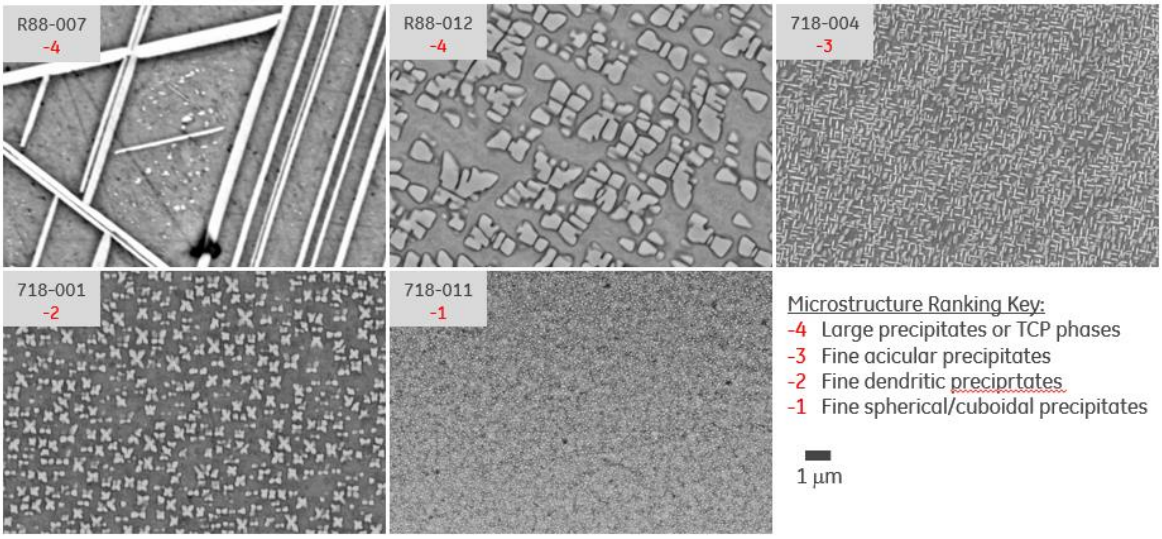

Figure 1: Typical examples showing a range of undesirable (-4 rank) to desirable (-1 rank) precipitate microstructures produced following homogenization and slow cooling.

In particular, alloy 718-011 (categorizes as -1 in Fig. 1), contains very fine precipitates that are difficult to see at this magnification. This is an example of an alloy that successfully passed our screening test, and further analysis of this alloy will be presented later.

Using the microstructure ranking scale we designed a series of experiments to capture trends with Al, Ti, and Nb; three elements that play an important role in γ' and γ" phase formation. Alloys R88-001 through R88-011 and 718-001 through 718-011 were characterized to produce the ternary plots shown in Fig. 2. Higher (yellow-red) values in these plots tend to produce more desirable microstructures for the current program.

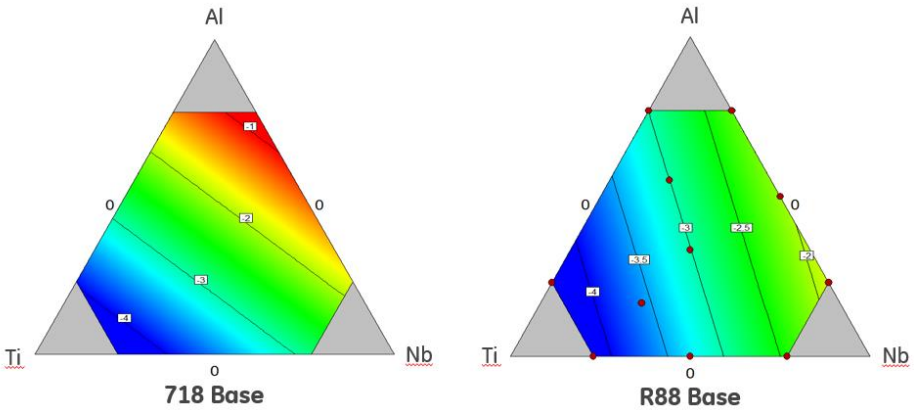

Figure 2: Microstructure rank plots for experiments in 718 and R88 based alloys (see Fig. 1 for rank key). Higher values tend to produce more desirable microstructures for the current program, i.e. fine γ' or γ'/γ" coprecipitates on slow cooling.

Note in both systems that high Ti levels generally lead to large precipitates and/or TCP phases; keeping Ti content low has been a consistently successful theme throughout this program. In the 718 based alloys, relatively high Al levels are preferred, while in the R88 based system higher Nb content tends to produce more desirable structures. These results reflect the overall strategy of moving a γ' forming alloy (R88) towards γ", and vice-versa for 718. More details on this design-of-experiments method and the alloys produced can be found in the Q1 (for 718) and Q2 (for R88) reports. The main outcome of this series of experiments was the identification of alloy 718-011, which produced a surprisingly fine γ' phase on slow cooling; more details on this alloy are contained later in this report.

In 1989 Andrieu, et al.[1] published a series of experiments on coprecipitation in 718-based alloys exploring "S-R" space, where S = Al + Ti + Nb is the total of all precipitate strengthening elements and R = (Al + Ti) / Nb is the ratio of γ' to γ" forming elements. This work was largely based on and extended the earlier work of Cozar, et al[2]. In both studies, alloys based on 718 are conventionally heat treated (solution treatment followed by rapid cooling to room temperature and age hardening) and then examined for γ'/γ" coprecipitation. An interesting result of the 1989 paper was the definition of a region in S-R space where compact coprecipitates are observed (cuboidal γ' with γ" on all six faces). In the present work, alloys 718-021 through 718-035 in Table 1 were designed to explore S-R space in a similar framework as Andrieu, et al., except that we subjected the alloys to slow cooling to test the concept of using coprecipitation to control γ' size. We also extended the previous work by exploring the effect of Ti/Al ratio, which was fixed at 0.5 by Andrieu, et al. In this study, we also evaluated ratios of 1.0 and 1.5. More discussion and details on the alloys produced can be found in the Q2 report, but a main outcome of this experimental series was the identification of alloy 718-027 which produced fine γ'/γ" coprecipitates on slow cooling. This alloy composition is in the center of the space defined by Andrieu, et al., and has a moderate Ti content.

Alloys 718-011 and 718-027 were both identified as potential candidates for large scale turbine forgings due to the fine γ' and γ'/γ" coprecipitates structures formed on slow cooling. TEM characterization of these alloys reveals the strengthening phases in more detail as shown in Fig. 3. Alloy 718-011 was observed to contain only γ' phase with a precipitate size around 50 nm. This result was somewhat surprising as we typically assume rapid coarsening kinetics for the γ' phase which would lead to overaging on slow cooling. However, with low Ti levels the γ' composition in alloy 718-11 was found to be rich in Al and Nb. It is speculated that limiting Ti increases Nb solubility in γ' and that this may be responsible for suppressing coarsening kinetics, leading to the fine ~50 nm precipitates. Increased Nb solubility in γ' may also explain why no γ" forms in this alloy on slow cooling. On the other hand, alloy 718-027, which contains relatively moderate levels of Al, Nb, and Ti, forms compact coprecipitates on slow cooling as seen in Fig. 3. The γ' portion of the coprecipitate is rich in Al and Ti, while the γ" phase is rich in Nb, as expected. While the precipitate size in alloy 718-027 is somewhat larger than in 718-011 (~100 nm vs. 50 nm), it is still in a range that should provide strengthening. Actual part cooling rates

[1] Andrieu, E., et al., Superalloy 718 – Met. & Applications, The Minerals, Metals & Materials Society, p241-256, 1989.
[2] Cozar, R., et al., Metallurgical Transactions, 4, p47-59, 1973.

will also be somewhat faster than those screened here, which will tend to produce finer precipitates in both alloys.

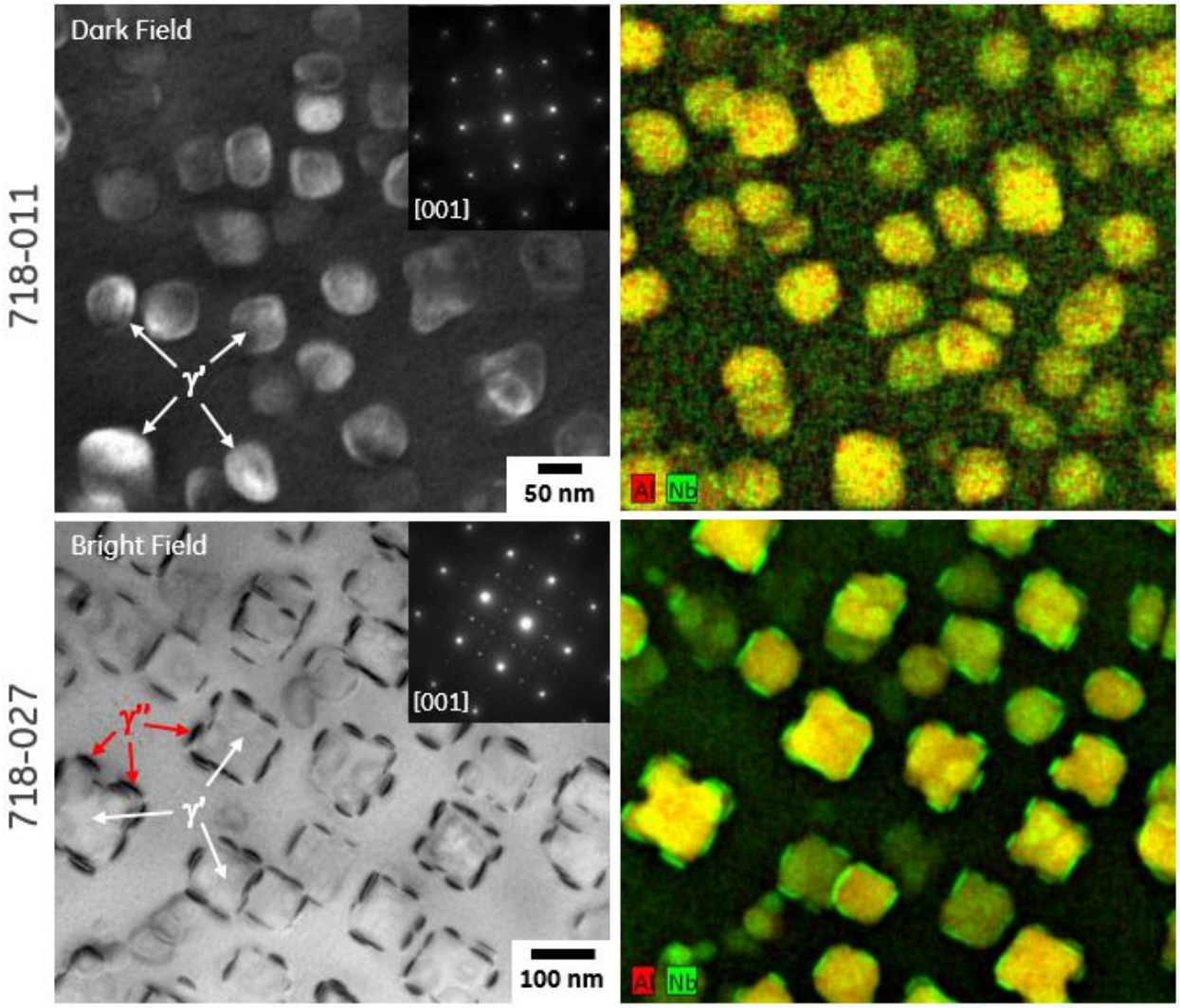

Figure 3: TEM images, SAD patterns, and EDS composition maps for alloys 718-011 and 718-027 showing fine γ' and γ'/γ" coprecipitates, respectively, following homogenization and slow cooling.

To further understand the transition in strengthening phases, and details on the coprecipitate sequence, we produced a series of alloys starting from baseline 718 and incrementally raising the (Ti+Al)/Nb ratio from 0.7 to a composition that strongly promoted γ′ formation (1.5). The (Ti+Al)/Nb ratios (and alloys) included in this study are 0.7 (baseline), 0.9 (718-036), 1.1 (718-037), 1.3 (718-038), and 1.5 (718-012). Typical microstructures from baseline and modified alloys are shown in Fig. 4 following homogenization and slow cooling. Baseline 718 contains γ″ with minimal nucleation of γ′. As expected, increasing the amount of γ′ forming elements produces larger γ′ precipitates. Interestingly, there was a noticeable inversion of the precipitation sequence as the (Ti+Al)/Nb ratio increased. The first phase to precipitate is normally the interior phase in a complex composite precipitate; at (Ti+Al)/Nb values of 0.7 and 0.9, the observations suggest γ″ precipitates form first and are decorated with numerous γ′ precipitates on cooling. At a (Ti+Al)/Nb

ratio of 1.1, γ′ and γ″ are of similar scale and number density with no clear preferred order, so their precipitation sequence is difficult to determine. It is likely that they nucleate at nearly the same time in the cooling sequence.

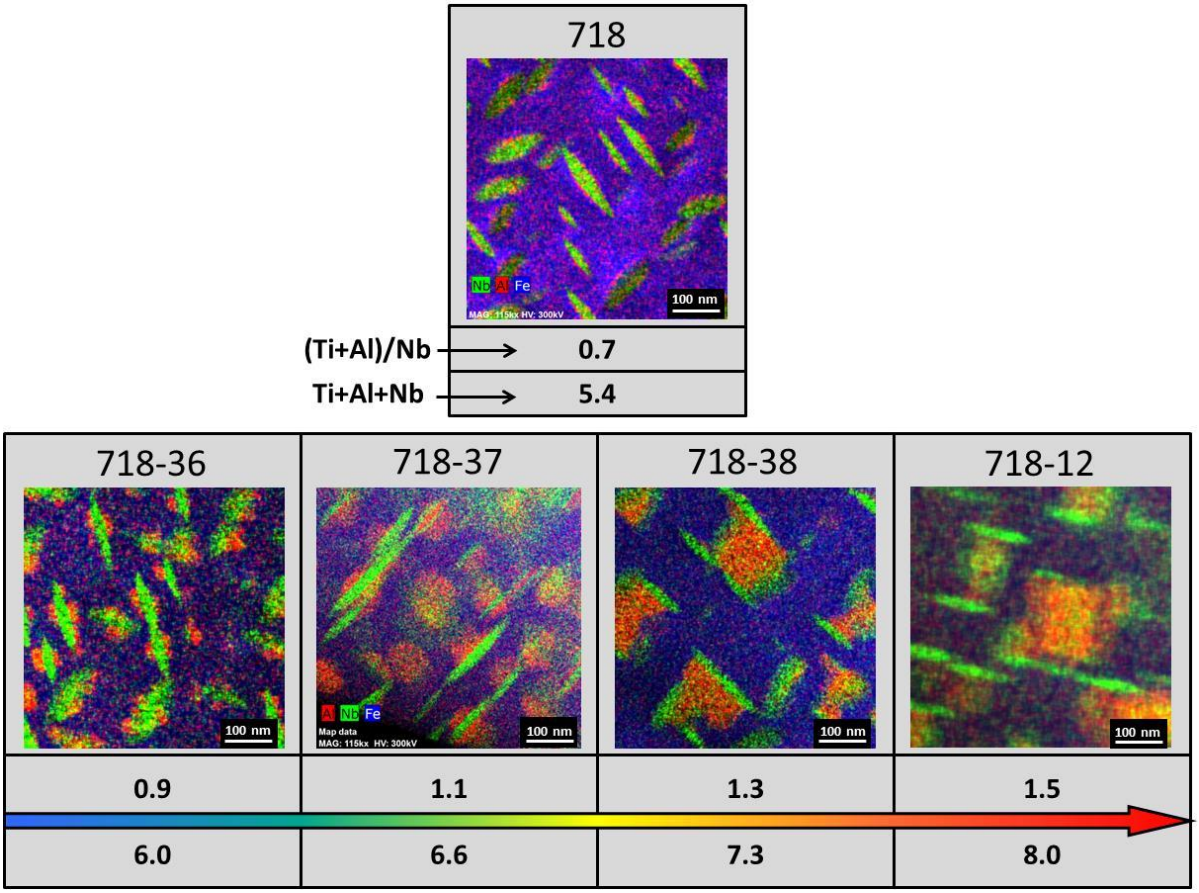

Figure 4: Typical microstructures of modified 718 alloys following slow cooling from homogenization where the (Ti+Al)/Nb has been incrementally raised to promote γ' formation (viewed on a <011> zone axis).

At higher (Ti+Al)/Nb values, the precipitation sequence reverses, and γ′ precipitates form with multiple γ″ on (001) faces. This demonstrated control over the nucleation sequence can be leveraged to optimize the size and morphology of γ'/γ" coprecipitates. Additional studies on the effect of Al/Nb ratio, Ti/Al ratio, and direct Ti addition to 718-011 are included in the Q3 report. Collectively, these investigations have been used to better understand the coprecipitation reaction and to identify a new alloy space where fine γ' only (without γ") is formed.

After screening all the alloys listed in Table I, 718-011 and 718-027 were selected for forging and heat treatment trials with the goal of producing fine grained samples for mechanical testing. All screening to this point was conducted on as-cast material with coarse grain size on the order of 1 mm. Multi-axis forging experiments where performed to refine the microstructure to an equiaxed grain size of ~10 μm. Figure 5 presents the final forging process sequence along with optical images of the resulting microstructure for baseline 718 and modified 718-011 and 718-027 alloys. Note the relatively uniform, equiaxed, fine grain structure across all alloys.

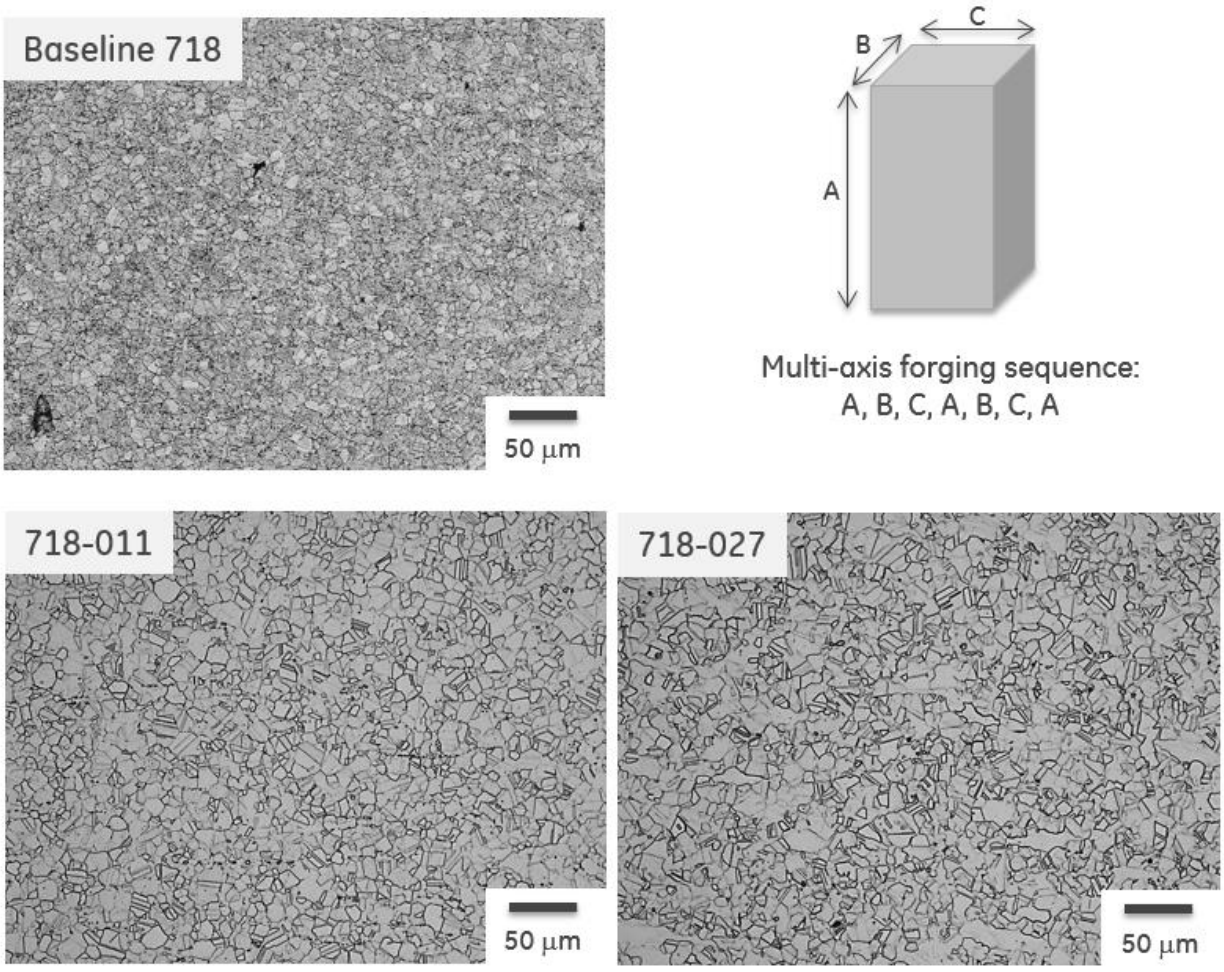

Figure 5: Multi-axis forging sequence used to billetize and pancake 718 and modified alloys 718-011 and 718-027 in preparation for heat treatment and mechanical property testing. Optical microscopy images confirm that this process successfully breaks down the as-cast ingot into a uniform, equiaxed, fine grained microstructure.

Following forging, a heat treatment study was performed to identify the optimal solution temperature for each alloy. Figure 6 presents the results of this study where microstructures are shown in the as-forged condition and after 1700˚F, 1800˚F, and 1900˚F exposure for 3hr. The correct solution temperature can be determined as the point where grain growth is observed (due to the dissolution of grain boundary pinning phases). For the modified alloys (718-011 and 718-027) 1800˚F/3hr was chosen as the solution temperature, while 1850˚F was selected for baseline 718 as this alloy was not fully solutioned at 1800˚F, and the highest temperature of 1900˚F was deemed excessive.

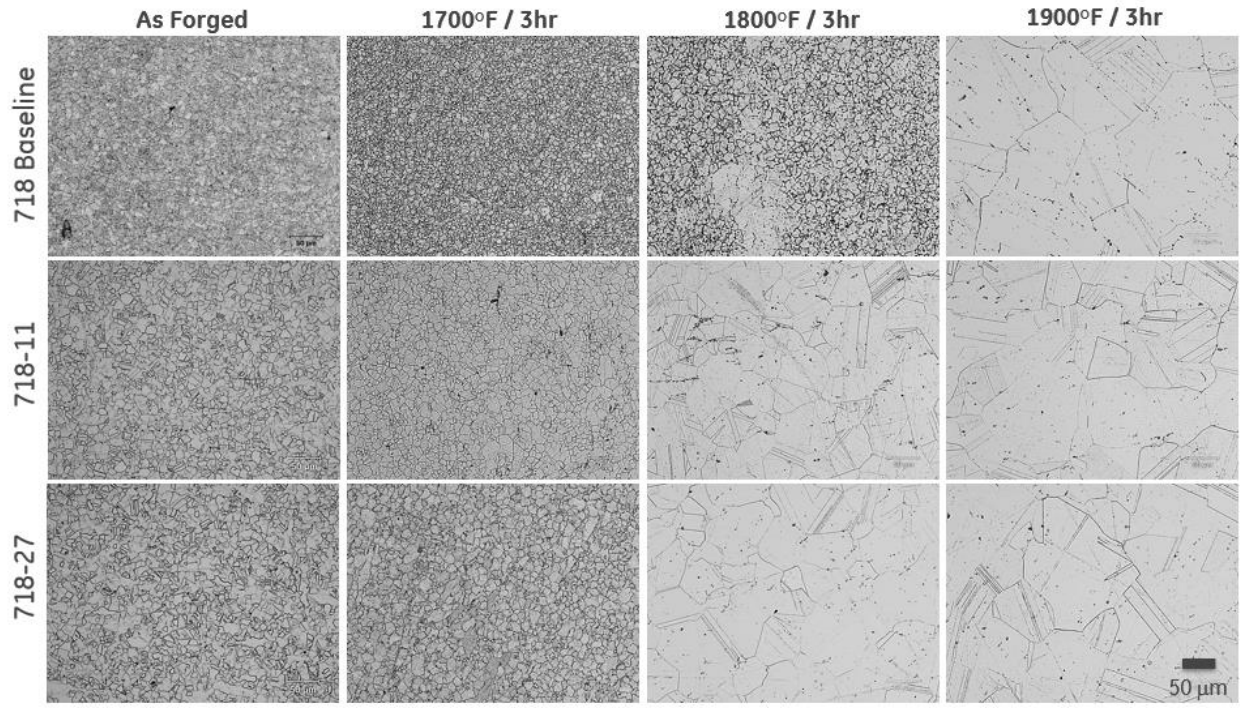

Figure 6: Optical images showing the grain structure in as-forged and solution treated samples of baseline 718 and alloys 718-11 and 718-27. Three different solution heat treatment temperatures were examined all at a fixed time of 3hr: 1700˚F, 1800˚F, and 1900˚F.

As a final step before preparing mechanical test specimens, an aging heat treatment study was conducted to increase alloy hardness and understand precipitation under faster cooling rates that simulate realistic part conditions. Hardness measurements were taken after cooling from homogenization at three different rates: two to simulate the predicted rate at rotor rim and bore locations, and a fast water quench. Hardness measurement were also taken after aging these samples at 1300˚F, 1400˚F, and 1500˚F for 8hr. A summary plot of all relative hardness data is shown in Fig. 7. The first set of measurements plots hardness in the as-homogenized state for 718 (blue), 718-011 (red), and 718-027 (green) arranged in order of decreasing cooling rate for each alloy. A clear trend appears across all three alloys – as-homogenized hardness increases with decreasing cooling rate. This is due to precipitation hardening that occurs on cooling from the homogenization temperature; slower cooling rates result in more precipitation and higher hardness. Among the three alloys, 718 shows the highest hardness, followed by 718-027 and 718-011 after bore simulative cooling. The next three groups of data show the effect of an 8hr age at 1300, 1400, and 1500˚F, keeping the same coloring scheme and grouping as described above. From the water quenched state all alloys show significant hardening following the three aging heat treatments with 1400˚F/8hr being the peak condition. At rim simulated cooling rates all alloys also age harden, but to a lesser extent; 1400˚F/8hr still appears to be the peak age condition. Results are mixed for the slowest rate examined here (bore simulative). Some hardening occurs at 1300˚F/8hr and 1400˚F/8hr for all alloys, but at 1500˚F/8hr minor softening occurs for 718 and 718-011.

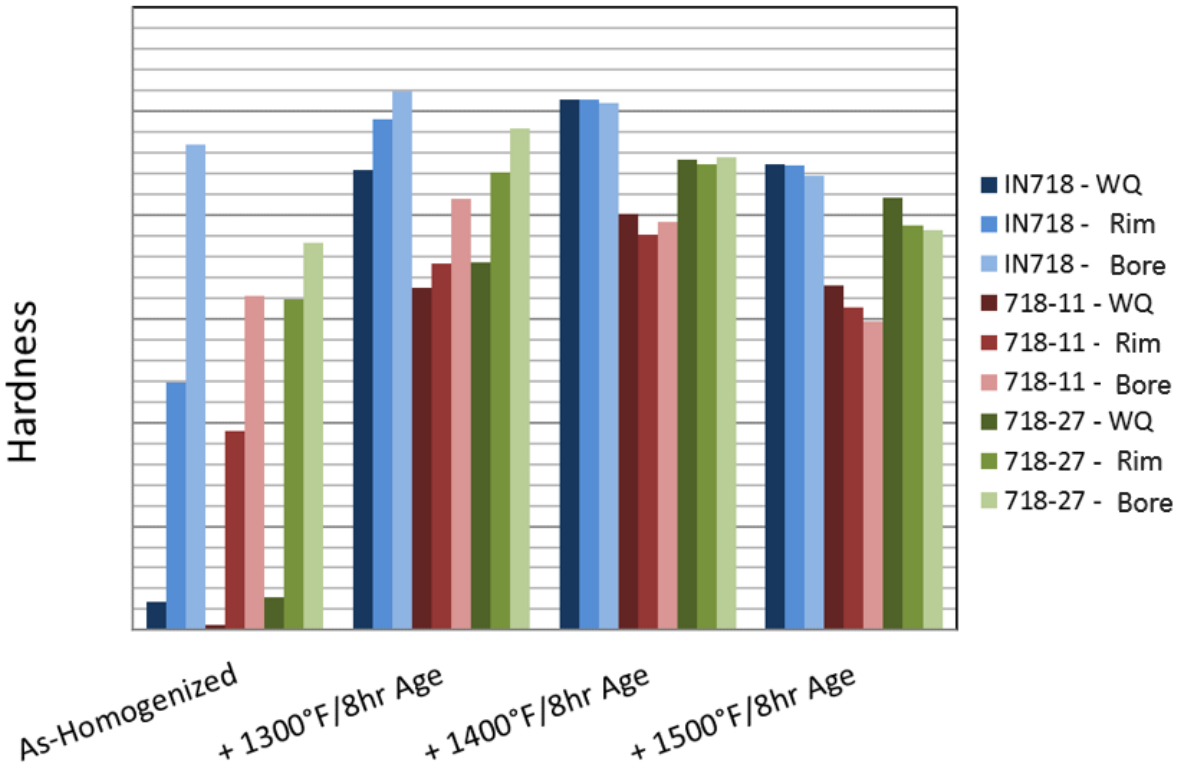

Figure 7: Relative hardness of baseline 718 and modified 718-11 and 718-27 alloys in the as-homogenized condition and after 8 hrs aging at 1300˚F, 1400˚F, and 1500˚F with three different cooling rates (water quench and rotor rim and bore simulative).

The combination of slow cooling plus high aging temperature apparently leads to an overaged condition for these alloys. Alloy 718-027 hardens negligibly following bore simulative cooling plus 1500˚F/8hr age. Based on these hardness results, 1400˚F/8hr provides the best overall aging response for all three alloys and was chosen as the aging condition for mechanical test specimens. Detailed TEM characterization was performed on a subset of the alloys and conditions discussed above to better understand the hardness trends. Results are summarized in the Q3 and Q4 reports where hardness is shown to correlate primarily with precipitate size.

In summary, a total of 67 alloys were melted, processed, and characterized to explore the use of γ'/γ'' coprecipitation and sluggish γ' precipitation to enable a next generation gas turbine rotor alloy. General trends and alloy design rules were revealed to produce fine strengthening precipitates on slow cooling to simulate large part processing conditions. Two candidate alloys were selected and subject to forging, solution heat treatment, and aging trials to produce samples for mechanical testing.

4.1.2 Coprecipitation Modeling

To gain a better understanding of the γ'/γ'' coprecipitation process, a multi-phase field (MPF) model was developed and combined with a commercial precipitation kinetics simulation software module, PanPrecipitation. Using these two models together enabled the coprecipitation

behaviors of γ' and γ'' precipitates from a supersaturated γ matrix to be studied for Alloy 718 and modified alloys produced during this project. Once validated, the unified model will enable rapid alloy chemistry modification to promote the desired compact coprecipitation.

The MPF model links directly with thermodynamic and atomic mobility databases and works at experimentally relevant time and length scales. In addition, the model treats the interactions and force balance at triple (or higher order) junctions where three individual phases meet together. Furthermore, the model incorporates interfacial energy anisotropy of all possible interfaces between the γ' phase and the three variants of the γ'' phase. Therefore, the MPF model is capable of investigating the influence of alloy chemistry and heat treatment conditions (such as aging temperature and cooling rates) on the precipitation sequence and thus the behavior of γ'/γ'' coprecipitates. PanPrecipitation is a built-in kinetic module in PANDAT software designed for simulating precipitation kinetics during heat treatment processes. It extends the capability of PANDAT beyond equilibrium thermodynamic calculations, while taking full advantage of both the automatic thermodynamic calculation engine (PanEngine) and the PANDAT Graphical User Interface. The simulations are carried out based on the built-in KWN (Kampmann-Wagner Numerical) model, which is capable of describing the concurrent nucleation, growth/dissolution, and coarsening process of multi-component alloys under arbitrary heat treatment conditions. Outputs of PanPrecipitation modeling include temporal evolution of nucleation rates, average particle size and number density, particle size distribution, volume fraction, and the composition of precipitates.

The two models work closely with each other to describe the coprecipitation reaction. Panprecipitation can be used for screening alloy compositions which may result in the coprecipitation reaction based on predicted precipitation sequence as characterized by the temporal evolution of nucleation rates. The calculated homogeneous nucleation rates of γ' and γ'' as a function of alloy composition during continuous cooling as well as isothermal aging can be used as input for the explicit nucleation algorithm in the MPF model. However, the Panprecipitation model describes the γ'/γ'' microstructure using one-point correlation functions (such as volume fraction and average particle size of each phase), which is neither sufficient to quantitatively define the microstructure (e.g. spatial correlations between γ'/γ''composite precipitates) nor capable of capturing heterogeneous nucleation of γ'' on γ' or vice versa (which needs to take long-range elastic interaction into account). These details, however, can be addressed quantitatively in the MPF model.

The models developed, and their outputs, are summarized in more detail in this section. The formulation of each model is described in detail in the quarterly reports. A parametric study on the stability of the γ'/γ'' coprecipitate structures was completed using the MPF model developed in Q1. The results showed the model's ability to predict the coprecipitated structures by varying the interaction between γ' and γ'' through interfacial energies. By manually seeding the γ'/γ'' coprecipition, the MPF simulation predicts the equilibrium shape of the coprecipitate with various configurations, including single lobe, $\gamma''/\gamma'/\gamma''$ sandwich, and compact (a cube-shaped γ' precipitate that has all six faces coated with a shell of γ'') morphologies. For each configuration, parametric studies have been carried out to investigate the stability of the composite precipitate under different combinations of interfacial energies. Figure 8 presents the equilibrium shapes of

a single lobe, sandwich, and compact structure using the following parameters: $\sigma_{\gamma'} = 50.5$, $\sigma_{\gamma''} = 101$ and $\sigma_{\gamma''/\gamma'} = 75.5\ (\mathrm{mJ/m^2})$.

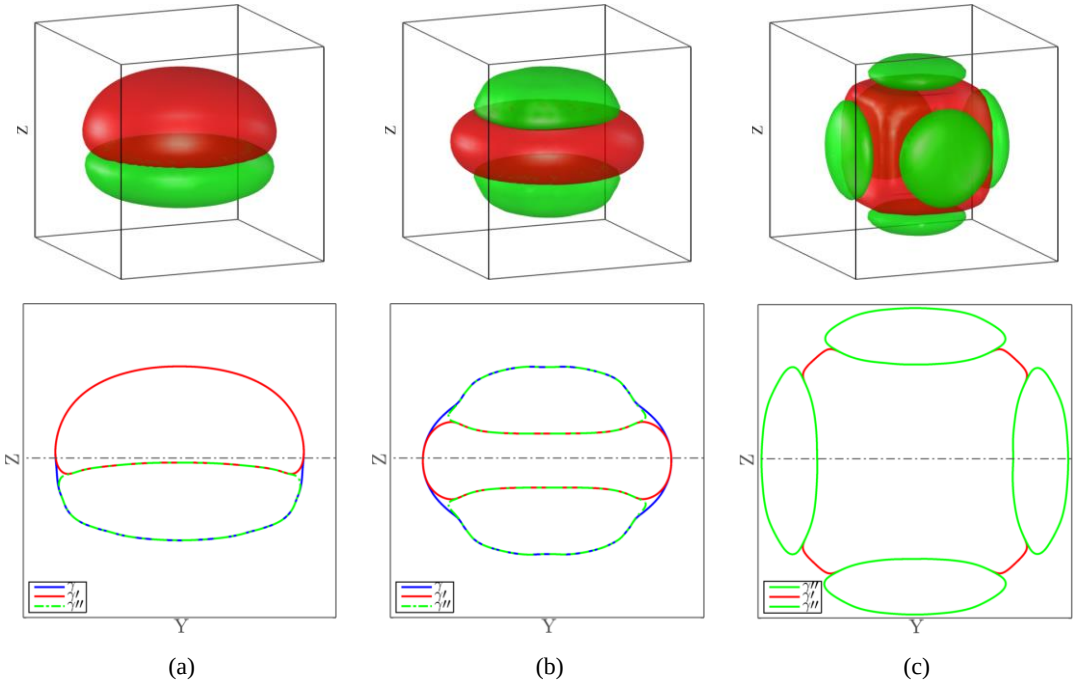

Figure 8: Equilibrium shapes for composite γ'/γ'' coprecipitates with different configurations using the energy combination of $\sigma_{\gamma'} = 50.5$, $\sigma_{\gamma''} = 101$ and $\sigma_{\gamma''/\gamma'} = 75.5\ (\mathrm{mJ/m^2})$. (a) Single lobe, (b) Sandwich, (c) Compact. The first row shows the composite particles in three-dimensions and the second row shows two-dimensional cross-sections along the yz plane through the center of the simulation box.

Here $\sigma_{\gamma'}$, $\sigma_{\gamma''}$, and $\sigma_{\gamma''/\gamma'}$ represent interfacial energies for the inter-phase boundaries of γ/γ', γ/γ'', and γ'/γ''phases, respectively. The γ'/γ'' interface is found to be non-flat, which suggested it was necessary to consider the strong interfacial energy anisotropy of the interface when compared with the flat γ'/γ'' interface observed in the experiments. Such a treatment in interfacial energy anisotropy was completed and described in the Q4 report.

The MPF model established in Q1 was also employed to study the growth behavior of γ'/γ'' coprecipitates. In particular, the influence of γ'' on the growth kinetics of γ' was investigated by making a direct comparison of the growth rate of the γ' phase while it is in direct contact with the γ'' phase (Figs. 9(a)-(b)), and when it is separated from the γ'' phase by a thin γ channel (Figs. 9(a')-2(b')). It was found that the growth of γ'' on the surface of γ' results in a strong growth and correspondingly a shape anisotropy of the γ' phase particle as described in the Q2 report. It was also found that γ'' coprecipiation on the surface of γ' significantly slows down the growth kinetics of γ'. The influence of γ'' on the growth kinetics also varies significantly with not only the configuration of coprecipitates but also the relative volume of γ' and γ'' particles in the same configuration. The compact structure is more efficient in reducing the growth kinetics of γ' when compared with the sandwich structure. In addition, the growth of γ' can be suppressed more effectively if the coprecipitate is formed early when the size of the γ' precipitates is small. The

underlying mechanism responsible for the decrease in γ' growth by γ" coprecipitation was determined via the analysis of the atomic flux vector of Al around γ' for both sandwich and compact structures.

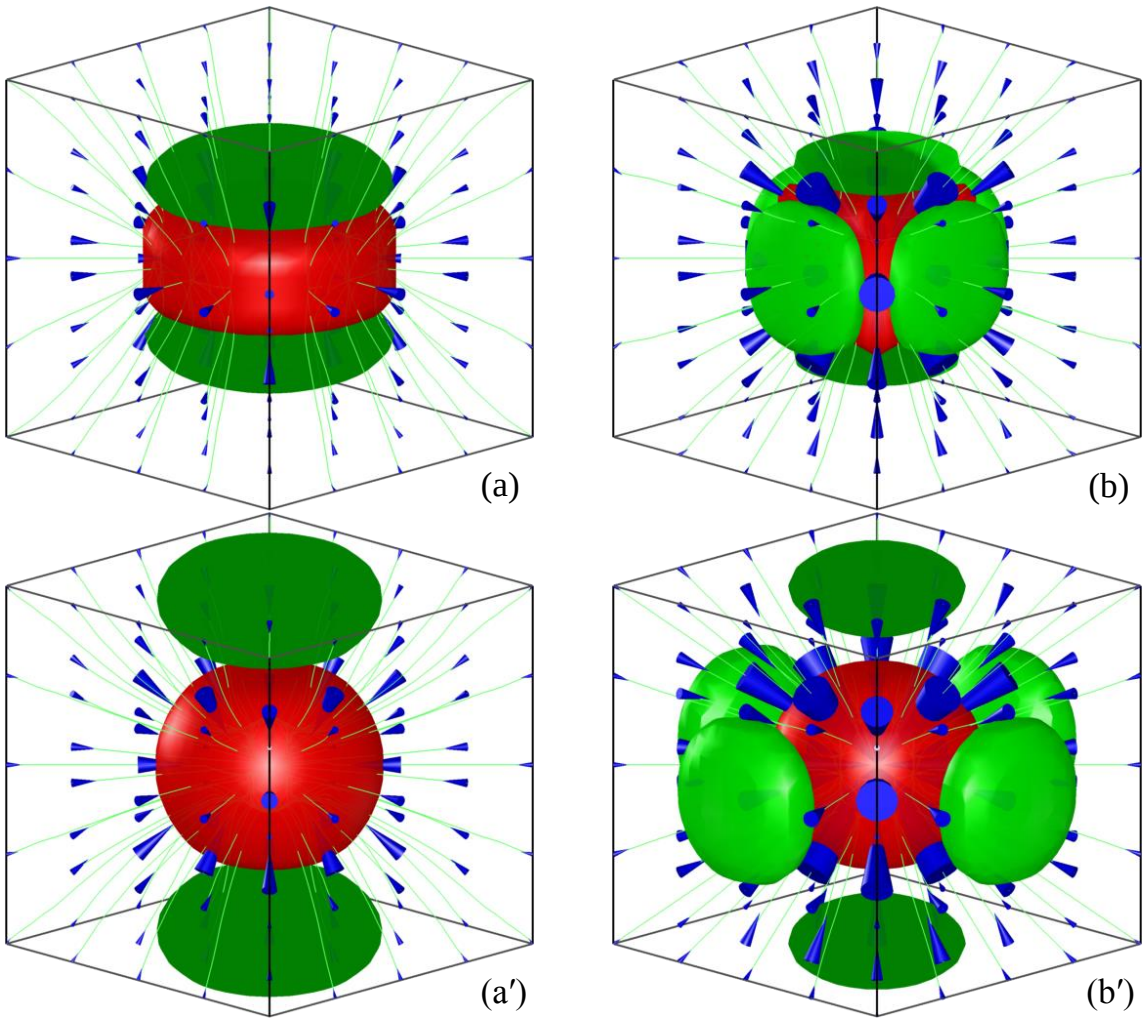

Figure 9: Analysis of atomic flux of Al during growth of γ' (red) and γ" (dark green) particles in the sandwich and compact co-precipitates. Flux vectors are plotted as blue cones in three-dimension in the direction of the flux vector as represented by the streamline in light green. The cones have their lengths proportional to the magnitudes of the flux vectors. In (a)-(b) γ' is in contact with γ" while in (a′)-(b′) they are separated.

The analysis showed that the decrease in growth rate is due (at least in part) to a diffusion barrier effect where γ" blocks the diffusional transfer of Al from the supersaturated matrix, preventing it from feeding the growth of the γ'. This is shown with the blue arrows around the γ' particle in both the coprecipiate and separate configurations that have a length proportional to the magnitude of the flux.

Precipitation of γ' and γ" (including precipitation sequence, size, and phase fraction) of three different 718-like alloys during continuous cooling were simulated with the PanPrecipitation module from Pandat software. Detailed simulation results for IN718, IN718-37 and IN718-38 are

provided in the Q3 report. The simulation results were in reasonable agreement with the experimental observations of the microstructure in terms of relative volume fractions and average size of the γ' and γ'' phases. Although only homogenous nucleation is considered in PanPrecipitation, the simulations can identify correctly the primary precipitate phase, showing that γ" precipitates out first in alloy 718 while γ' phase precipitates out first in alloy 718-38. PanPrecipitation modeling of the precipitation sequence during isothermal aging in IN718-37 and IN718-38 has been validated with experimental observations. Diffraction analysis of phases present in IN718-37, when aged for different duration at 1456°F following a super-solvus heat treatment and water quench, confirmed the precipitation sequence predicted by the model. The prediction and diffraction patterns as a function of aging time are shown in Figure 10.

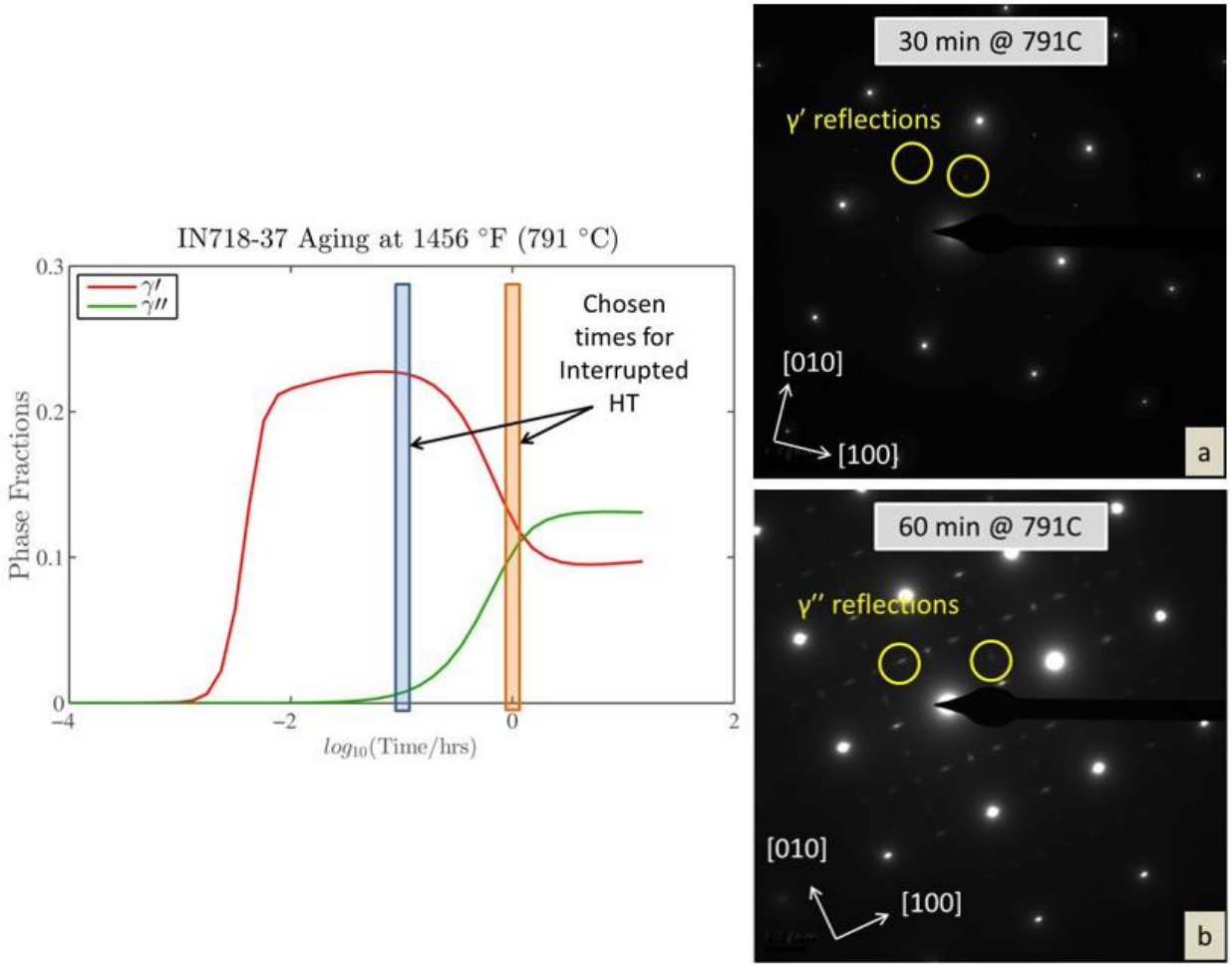

Figure 10: Expected phase fraction of γ′ and γ″ during a heat treatment at 791°C based on precipitation modeling. The [001] diffraction patterns for samples (a) 30 min 791°C and (b) 60 min @ 791°C showing diffraction spots from γ′ in (a) and both γ′ and γ″ in (b).

The capability of PanPrecipitation to correctly predict precipitation sequence is important in that it can help narrow down the composition range and heat treatment procedure for more efficiently screening alloys which have coprecipitation reactions.

Coprecipitation upon continuous cooling has been successfully simulated in a pseudo-ternary system using a modified MPF model (with temperature dependence and interfacial energy anisotropy for the γ'/γ'' interfaces) for two different alloy compositions: Ni-2.4Al-3.8Nb and Ni-2.4Al-2.0Nb (at.%). According to PanPrecipitation kinetics modeling, upon slow cooling (i.e. equilibrium condition) and fast cooling (e.g. 50°F/s), γ" will precipitate out first followed by γ' for Ni-2.4Al-3.8Nb, and the opposite is true for Ni-2.4Al-2.0Nb. Depending on precipitation sequence, sandwich coprecipitates ($\gamma'/\gamma''/\gamma'$) in Ni-2.4Al-3.8Nb or incomplete compact coprecipitates in Ni-2.4Al-2.0Nb (i.e. 3 faces of the γ' precipitate are coated with γ'') have been observed as was detailed in the Quarter 4 report. The formation of coprecipitates with different configurations results from the heterogeneous nucleation of secondary precipitates on the surface of the primary precipitates. The exact heterogeneous nucleation sites of γ' on γ'' and γ'' on γ' are at the γ-matrix side of the interface because of the enrichment of solute elements rejected by the pre-existing growing precipitates. This model allows for prediction of the type of coprecipitates ("sandwich" or "compact") as a function of alloy composition, aging temperature, and cooling rates.

In summary, a multi-phase field model of the coprecipitation of γ'/γ" has been developed and combined with PanPrecipitation to investigate γ'/γ" coprecipitation behavior in a Ni-Al-Nb pseudo-ternary system, including:

1) The equilibrium shape of γ'/γ'' coprecipitates with different configurations including single lobe, sandwich, and compact morphology.
2) The growth behavior (shape and kinetics) of γ'/γ'' coprecipitation with different initial configurations during isothermal aging and, in particular, the influence of γ" on the growth kinetics of γ' and its dependence on the configurations of coprecipitates.
3) The coprecipitation process upon isothermal aging and during continuous cooling as a function of alloy composition.
4) Formation mechanisms of different types of coprecipitates and their dependency on alloy composition and aging temperature.

The modeling work resulted in a better understanding of the experimental coprecipitation work and it has been concluded that:

1) The growth kinetics of γ' in the compact coprecipitate configuration is significantly slower than that of individual (monolithic) γ' precipitates.
2) The growth of γ' can be suppressed more effectively if the coprecipitate is formed early, when the size of γ' is still small.
3) The reduced growth rate of γ' in the compact configuration is likely due to a decrease in Al flux directly caused by the presence of γ'' coprecipitation.
4) The alloy composition and cooling rate plays a critical role in determining the coprecipitation process, leading to different coprecipitate configurations.
5) Pre-existing γ' or γ'' precipitates are able to promote heterogeneous nucleation of γ'' or γ' on its surface, leading to the formation of coprecipitates. The most favorable nucleation sites for γ' on γ'' and γ'' on γ' are found to be at the γ-matrix side of the interface because of the enrichment of solute elements rejected by the pre-existing growing precipitates.

6) Interfacial energies between different phases (γ, γ', and γ'') play a critical role in determining the equilibrium shape (e.g. such as contact angles at three-phase junctions).

4.2 Oxide Dispersion Strengthening

Over the course of the program, 92 mill runs were completed comprising 29 different milling parameters or chemistries as detailed in Table 2. All runs were completed on a starting base chemistry of either Alloy 1 or Alloy 2.

Milling Condition ID	Quarter Milled	Alloy	Oxide Loading	Metallic Element 1 Loading*	Metallic Element 2 Loading	Milling Rotational Speed	Milling Time	PCA	Total Yield (%)	Useable Yield (%)
N1	Q1	Alloy 1	1x	1y	--	A	2	--	98	~98
N2	Q1	Alloy 1	1x	2y	--	A	2	--	95	~95
N3	Q1	Alloy 1	1x	1y	--	B	1	--	97	~97
N4	Q1	Alloy 1	1x	2y	--	C	1	--	62	59
N5	Q1	Alloy 1	1x	2y	--	D	1	--	53	46
N6	Q1	Alloy 1	1x	1y	--	E	1	--	45	38
N7	Q1	Alloy 1	1x	1y	--	E	2	--	36	22
N8	Q1	Alloy 1	1x	1y	--	F	1	--	42	35
N9	Q1	Alloy 1	1x	1y	--	F	1	P	92	85
N10	Q1, Q2	Alloy 1	1x	2y	--	F	1	--	49	32
N11	Q1	Alloy 1	1x	4y	--	F	1	--	55	42
N12	Q1	Alloy 1	1x	2y	2z	F	1	--	62	50
N13	Q1	Alloy 1	1x	--	1z	F	1	--	41	28
N14	Q1	Alloy 1	1x	--	2z	F	1	--	44	33
N15	Q1	Alloy 1	1x	--	4z	F	1	--	26	17
N16	Q2	Alloy 1	2x	4y	--	F	1	--	64	52
N17	Q2	Alloy 1	3x	6y	--	F	1	--	34	27
N18	Q2	Alloy 2	--	10y**	--	F	1	--	70	22
N19	Q2	Alloy 2	1x	10y**	--	F	1	--	46	30
N20	Q2	Alloy 2	2x	10y**	--	F	1	--	76	63
N21	Q2, Q3	Alloy 2	2x	10y**	1z	F	1	--	61	40
N22	Q2	Alloy 2	2x	10y**	2z	F	1	--	51	36
N23	Q2	Alloy 2	2x	10y**	4z	F	1	--	59	43
N24	Q3	Alloy 1	1x	4y	--	G	1	--	55	24
N25	Q3	Alloy 1	2x	4y	--	F	2	--	81	67
N26	Q3	Alloy 1	2x	4y	--	G	1	--	52	34
N27	Q3	Alloy 2	2x	10y**	1z	F	2	--	12	3
N28	Q3	Alloy 2	2x	10y**	1z	G	1	--	11	1
N29	Q4	Alloy 1	0.5x	1y	--	G	1	--	61	28

Table 2: Milling details for Alloy 1 milled with Praxair powder & Alloy 2 milled with CarTech Powder.
(*Alloy 1 powder contained 0.5y pre-alloyed)
(Alloy 2 contains 10y pre-alloyed, no additional "y" is doped into the alloy for these trials)**

These two bases were chosen because they have excellent hold time fatigue crack growth resistance but have too low a strength to be used as wheel materials. The mill runs focused on identifying the optimal milling processing conditions as well as varying the type and quantity of alloy dopants to achieve the optimal nano-oxide morphology and distribution.

The initial milling goal was to identify processing conditions which provided a balance between decreasing useable powder yield and improving microstructure and nano-oxide distribution. Higher milling energy, via either higher speeds or longer milling times (or both), was desired to best incorporate dopants and starting oxides. However, as the milling energy was increased, the amount of powder galling increased leading to powder adhering to milling media and internal mill surfaces. This resulted in a lower useable powder yield. A series of small as-HIP structures were analyzed via TEM to assess the nano-oxide precipitation as a function of milling parameters. Based on the size and number density of oxides seen, along with the useable powder yield, initial mill parameters (parameter F1) were chosen. However, more detailed subsequent analyses including both low and high magnifications showed significant levels of unincorporated dopants to be present (Figure 11).

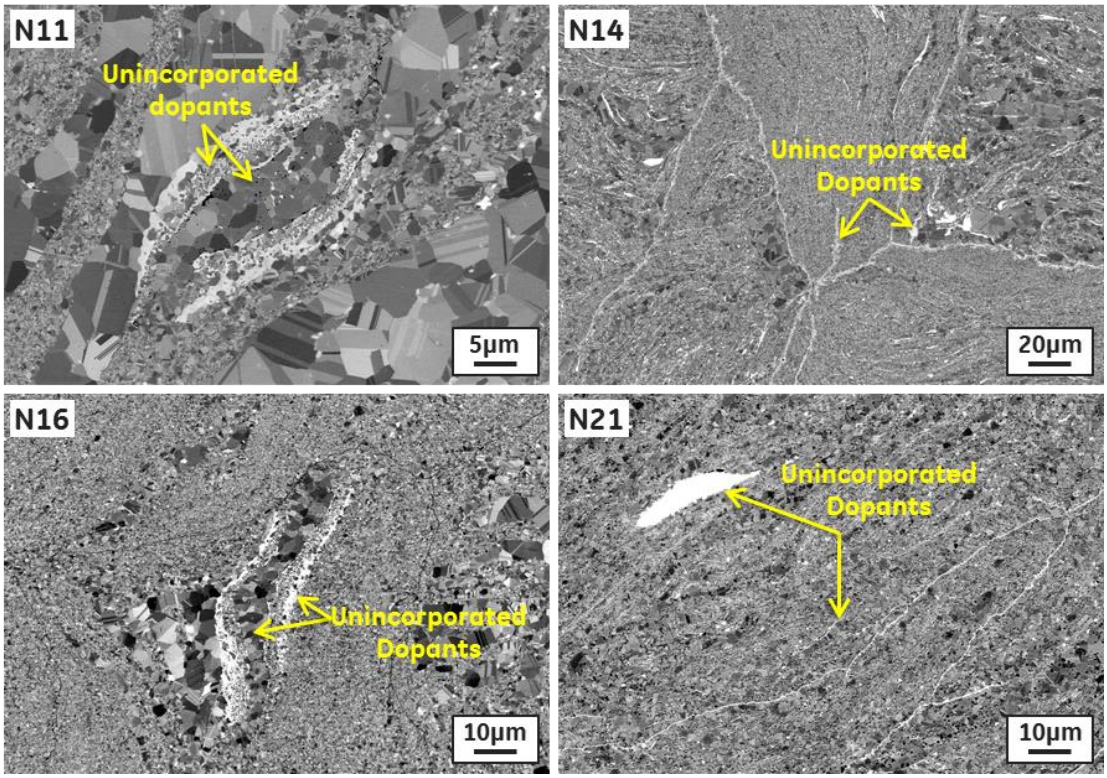

Figure 11: SEM images of unincorporated dopants visible in both Alloy 1 and Alloy 2 due to insufficient milling energetics. This could be detrimental to properties.

Having significant levels of unincorporated dopants is detrimental to properties because it negatively impacts the nano-oxide precipitation density and creates inhomogeneous regions that are likely more brittle than the matrix. Further milling trials were completed at either higher rotational speed or longer times and new milling parameters (parameter G1) were chosen. The higher energy trials did decrease the amount of unincorporated dopant contamination; however, there was still some contamination visible (Figure 12) and the useable powder yield decreased significantly. Because these trials indicated that even higher milling energetics may be necessary to fully incorporate all dopants, further work should pre-alloy all metallic components during gas atomization such that the milling only needs to fully dissolve the starting oxide component.

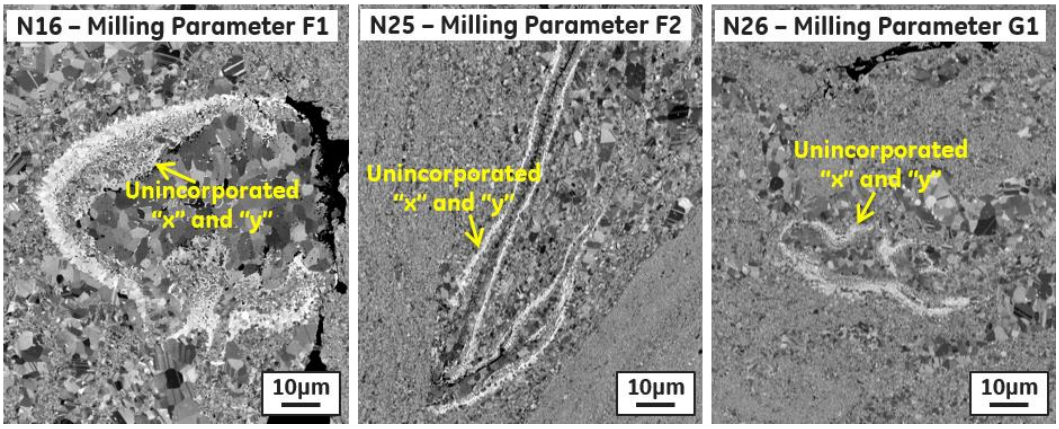

Figure 12: SEM images of Alloy 1 showing contamination from unincorporated dopants during milling. The quantity of contamination did decrease with increasing milling energetics.

For more details regarding milling energetics please refer to the Q1 report for the initial parameter selection and the Q4 report for the higher milling energetics evaluation.

Following milling process parameter optimization, the focus was to screen chemistry modifications and identify the chemistry system which yielded the desired nano-oxide distribution for each alloy. Table 3 details the chemistry systems evaluated for each alloy.

Milling Condition ID	Alloy	Oxide Loading	Metallic Element 1 Loading*	Metallic Element 2 Loading
Set 1: Vary "y" Loading with constant 1x oxide loading				
N8	Alloy 1	1x	1y	--
N10	Alloy 1	1x	2y	--
N11	Alloy 1	1x	4y	--
Set 2: Effect of "y" and "z" Loading with 1x oxide loading				
N12	Alloy 1	1x	2y	2z
Set 3: Vary "z" Loading with constant 1x oxide loading				
N13	Alloy 1	1x	--	1z
N14	Alloy 1	1x	--	2z
N15	Alloy 1	1x	--	4z
Set 4: Vary Loading with Constant x/y Ratio				
N29	Alloy 1	0.5x	1y	--
N10	Alloy 1	1x	2y	--
N16	Alloy 1	2x	4y	--
N17	Alloy 1	3x	6y	--
Set 5: Effect of Milling on γ'				
N18	Alloy 2	--	10y*	--
Set 6: Vary "x" Loading				
N19	Alloy 2	1x	10y*	--
N20	Alloy 2	2x	10y*	--
Set 7: Vary "z" Loading with constant 2x oxide loading				
N21	Alloy 2	2x	10y*	1z
N22	Alloy 2	2x	10y*	2z
N23	Alloy 2	2x	10y*	4z

Table 3: Chemistry modifications evaluated for Alloy 1 and Alloy 2.
(*Alloy 1 contains 0.5y pre-atomized into the alloy)
(*Alloy 2 contains ~20y pre-atomized, no additional "y" was doped into the alloy for these trials)

ODS feasibility was demonstrated for both Alloy 1 and Alloy 2. Based on a finer size and more homogeneous precipitation, “y” additions in Alloy 1 were shown to be a more effective dopant than “z” (Figure 13).

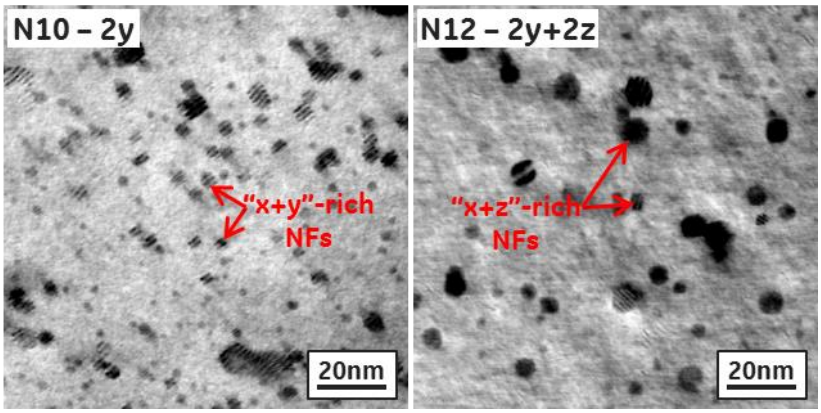

Figure 13: TEM images of samples N10 and N12 showing the increase in size and decrease in number density of the nanometer sized oxides (nano-oxides) with the inclusion of “z” in Alloy 1.

By varying the “x” and “y” levels, the size and distribution of these nano-oxides can be tailored (Figure 14) to try to achieve an optimal balance of properties.

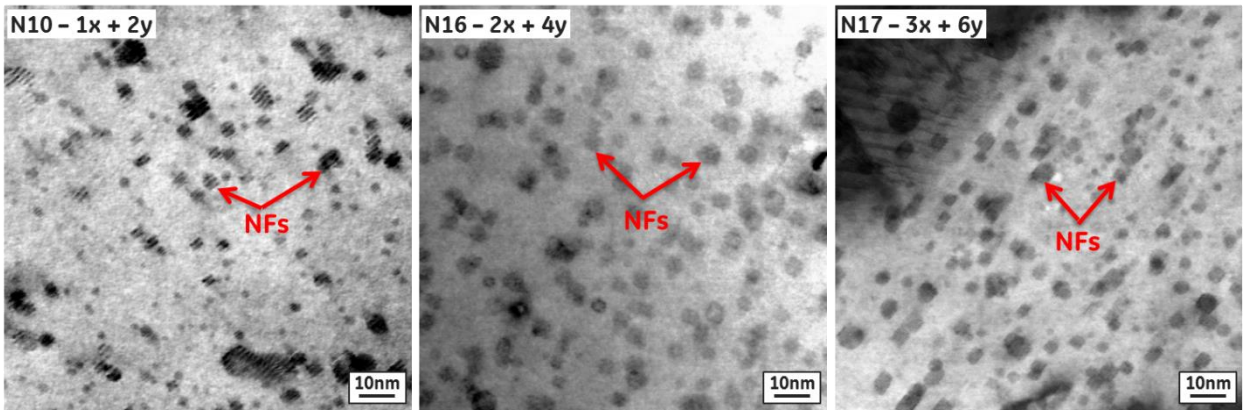

Figure 14: TEM analysis showing the increase in nano-oxide precipitation when increasing both the “x” and “y” levels with milling parameters F for time 1.

Despite being able to demonstrate that the nano-oxide distribution can be changed, all mechanical properties tested during this Phase 1 program occurred only on the original milling parameters. The mechanical property evaluation details are described in Section 4 and show that oxide dispersion strengthening Alloy 1 via the incorporation of 1x and 2y significantly increased the yield strength as compared to baseline PM Alloy 1 and far surpassed the strength necessary for use as a wheel material. However, the low ductility indicated that the oxide dispersion strengthening needed to be reduced to achieve a better balance of properties.

The second alloy investigated was the γ' strengthened Alloy 2. To drive the γ' precipitation, Alloy 2 contains approximately 1.5wt% Al. As discussed in literature[3], Al has been seen to poison the nano-oxide reaction forming coarser Al-"x" based nano-oxides that are less effective at dispersion strengthening. Thus, "z" additions were investigated as they have been reported to prevent the formation of Al-"x" nano-oxides and instead form finer "z"-"x" based nano-oxides[4,5]. First, Alloy 2 was milled with only "x" additions (1x or 2x) to understand whether the pre-alloyed "y" could be used to effectively precipitate nano-oxides or whether the pre-alloyed Al content would prevent this reaction from occurring. SEM and TEM evaluation of this material shows that both γ' and nano-oxides are present and act as pinning phases resulting in a finer grain size than the baseline PM Alloy 2. However, the EDS results as seen in Figure 15 clearly show that the nano-oxides are associated with Al and "x", not "y" and "x", as desired.

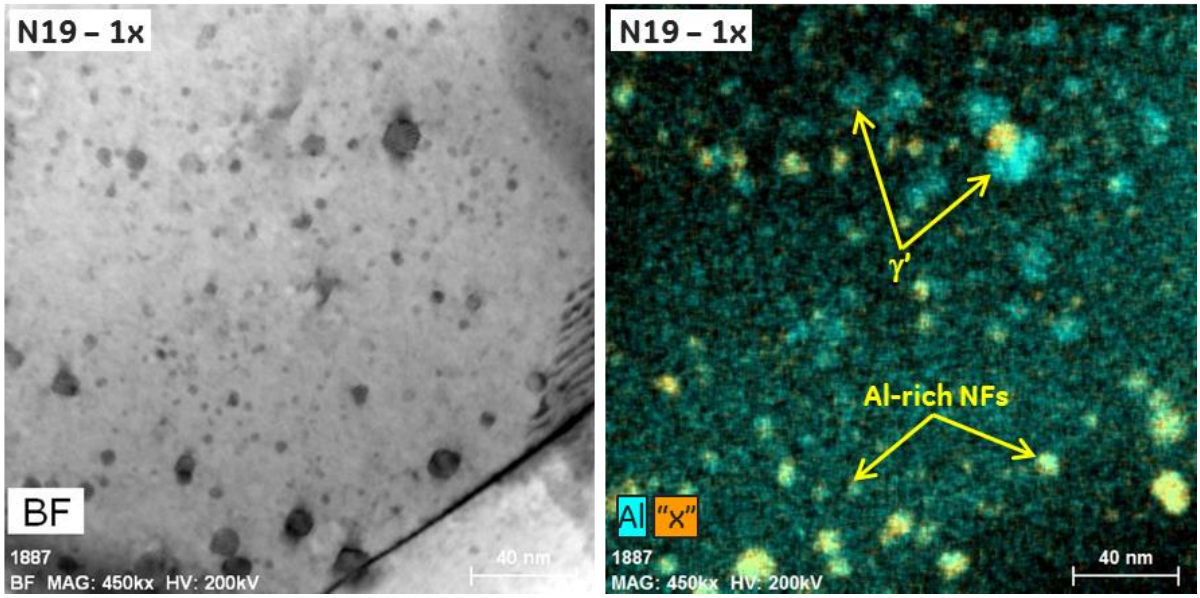

Figure 15. (a) Bright field TEM image and (b) EDS map showing the Al-"x" containing NFs and the γ' formed in Alloy 2 with 1x oxide loading.

Thus, despite their fine size, the Al has prevented the intended "y"-"x" nano-oxide from forming. Further, the inclusion of Al in the nano-oxides means that the γ' chemistry has likely been changed. While the loss of Al available may not be enough to change the γ' volume fraction significantly, it could have a significant effect on the γ' misfit stress which, in turn, can have a negative impact on the mechanical properties. When "z" was added, there was no longer Al association with the nano-oxides. Rather, the nano-oxides are "z"-"x" based and the Al is segregated only to the γ' as shown in Figure 16. Even though "z" has been effective at preventing the Al segregation to the nano-oxides, the resulting "z"- "x" nano-oxides are coarser than the Al-"x" nano-oxides.

[3] G.B. Schaffer, M.H. Loretto, R.E. Smallman, J.W. Brooks. 1989. Acta Met. 37: 2551-2558.
[4] S.M. Seyyed Aghamiri, H.R. Shahverdi, S. Ukai, N. Oono, K. Taya, S. Miura, S. Hayashi, T. Okuda. 2015. Mat. Char. 100: 135-142.
[5] Q. Tang, S. Ukai, N. Oono, S. Hayashi, B. Leng, Y. Sugino, W. Han, T. Okuda. 2012. Mat. Trans. 53: 645-651.

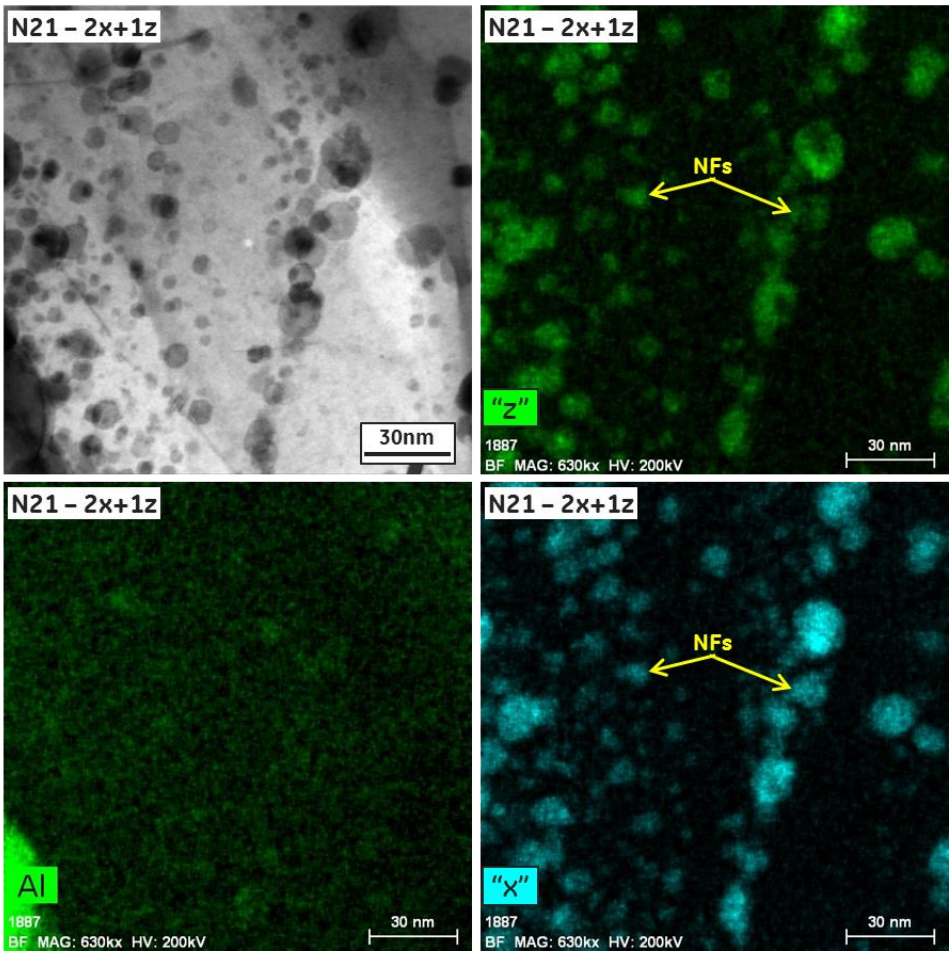

Figure 16. Bright field TEM image and EDS maps showing that the addition of metallic dopant "z" leads to "z"-"x" rich NFs with no Al association in Alloy 2.

As the quantity of "z" increased from 1z to 2z to 4z, the amount of nano-oxides did increase. However, the large grain area fraction and the quantity of unincorporated dopants increase as well so the focus was on lower "z" quantities. Mechanical properties were evaluated for the baseline PM Alloy 2 and Alloy 2 with 1z+2x. As was true for Alloy 1, the ODS Alloy 2 resulted in a large increase in strength and a large decrease in ductility. This shows that a lower oxide loading is required to achieve the necessary balance of properties. For more details regarding the Alloy 2 chemistry modifications please refer to the Q2 and Q3 reports.

The final focus was to screen thermo-mechanical processing conditions to identify the optimal processing conditions. This work focused on evaluating the effect of HIP temperature, forge temperature, and post-forge heat treatments. In both Alloy 1 and Alloy 2 ODS samples, increasing the HIP temperature led to a decrease in the as-HIP porosity; however, the grain size and the quantity of large grains increased as seen for Alloy 2 in Figure 17. The increased grain size will result in a reduction in the strength as the Hall-Petch strengthening is decreased. Increasing the HIP temperature in Alloy 1 also led to a decrease in the quantity of delta phase present as the delta solvus temperature was approached or surpassed. In the case of Alloy 2, the sub-solvus processing showed that the fine-grained region was made up of alternating bands defined by

grain size and primary γ' precipitation as seen in Fig. 17a. Where there was a greater density of primary γ', the grain size was finer. This banded structure was not seen in the baseline consolidation.

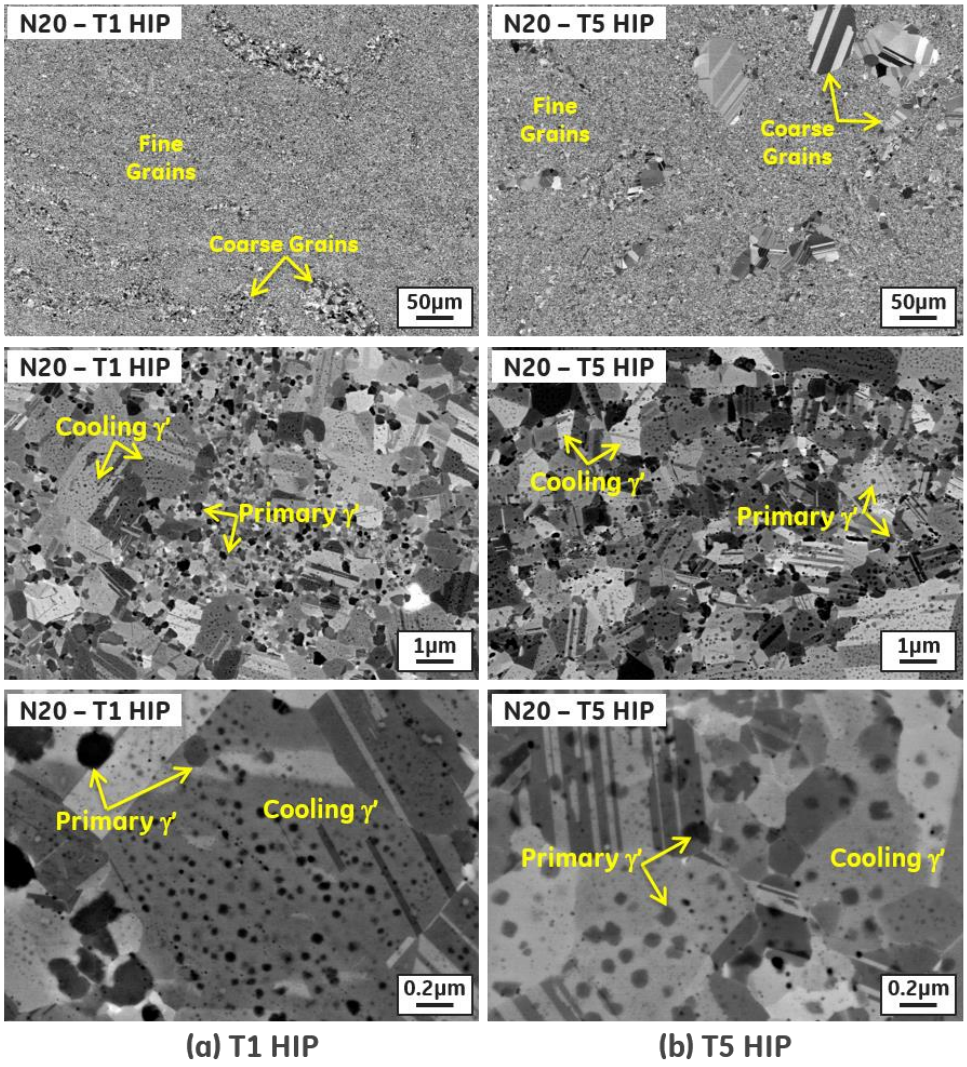

Figure 17: SEM images of Alloy 2 containing 2x "x" (N20) showing the change in microstructure and γ' distribution when the HIP temperature is increased from (a) sub-solvus HIP to (b) super-solvus HIP.

Thus, milling is changing the primary γ' distribution and this is leading to a different sub-solvus microstructure. Increasing the HIP temperature to a super-solvus temperature increased the γ' size and resulted in a more homogeneous distribution of the γ' as opposed to the banded structure seen in the sub-solvus HIP samples (Fig. 17b).

However, in both Alloy 1 and Alloy 2, increasing the HIP temperature also led to coarsening of the nano-oxides as seen in Figure 18. Previously completed work on nanostructure ferritic alloys (NFAs) at GRC showed no coarsening of the nano-oxides below 2400°F. It is not known what is leading to the coarsening of nano-oxides in Alloy 1 and Alloy 2 with elevated temperatures. In

the case of NFAs, the nano-oxides formed are of the “y”-“x” type and are very stable. It is possible that the incorporation of Al into the Alloy 2 nano-oxides and Alloy 2 N20 nano-oxides have altered this stability allowing for nano-oxide coarsening at lower temperatures. Alloy 2 N22 containing “z”, showed a more significant increase in nano-oxide size at elevated temperatures indicating the “z” containing nano-oxides are not as stable as the “y”-based nano-oxides.

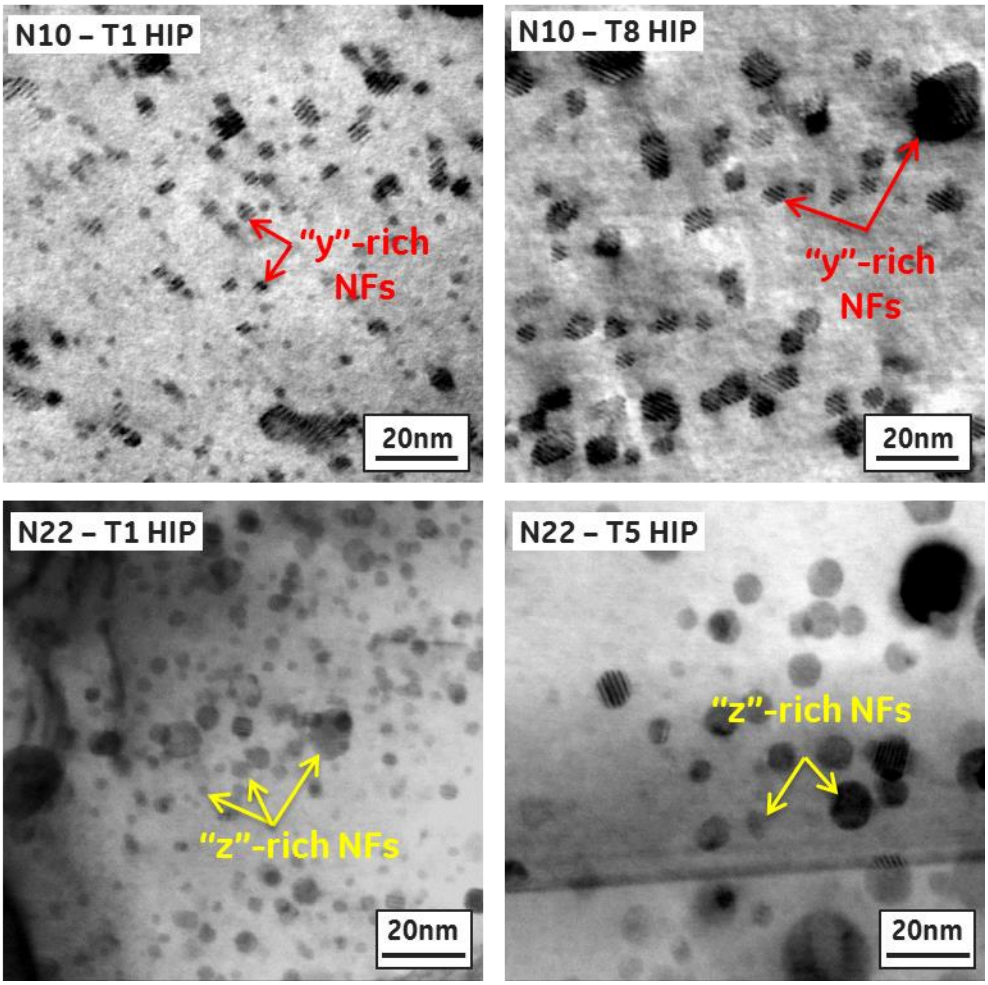

Figure 18: TEM images depicting the coarsening of the nano-oxides at higher HIP temperatures in both Alloy 1 (N10) “y”-based nano-oxides and the Alloy 2 (N22) “z”-based nano-oxides.

Another possibility is that the change in matrix from a BCC structure to an FCC structure changes the precipitate/matrix interface properties allowing for more rapid coarsening. Coarsening of the nano-oxides could be detrimental to the dispersion strengthening which relies on the dense distribution of fine nano-oxides.

Forging the baseline PM Alloy 1 and PM Alloy 2 alloys at temperature T1 led to a decrease in the grain size compared to the as-HIP structure. In the case of the ODS samples, forging decreased the large grain size; however, the fine grain size increased as compared to the as-HIP structure as shown in Figure 19.

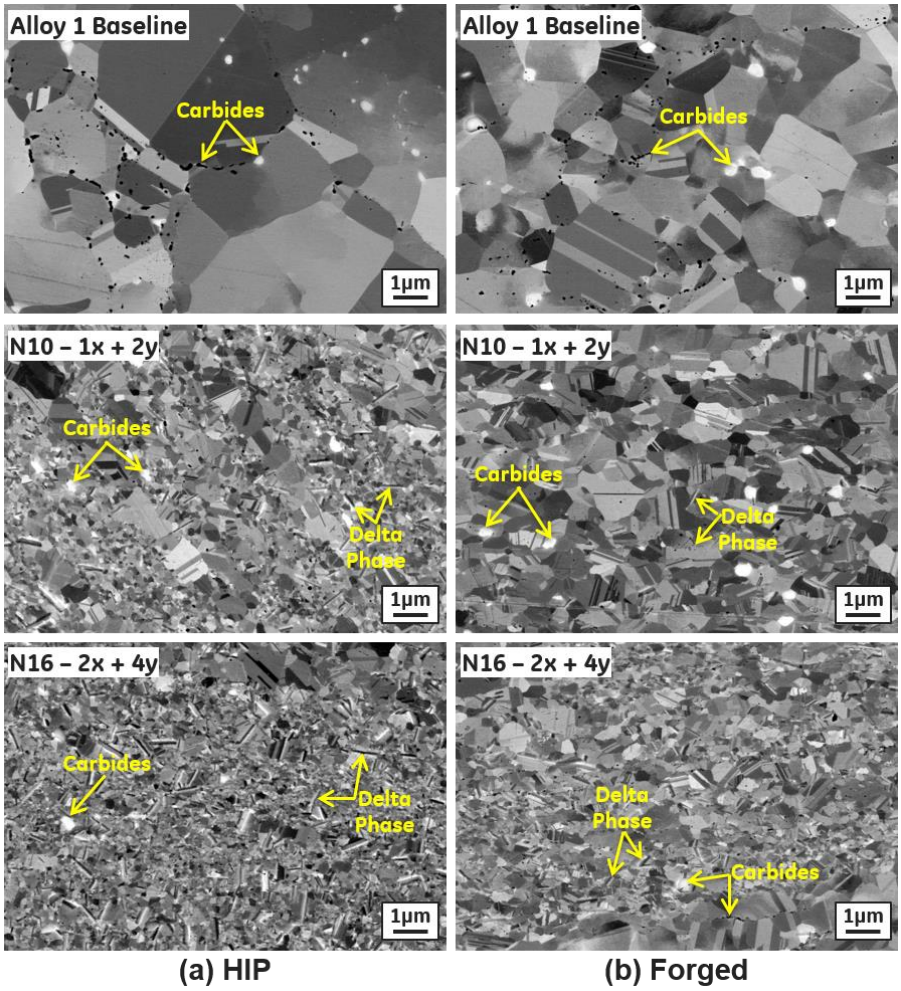

Figure 19: SEM images of Alloy 1 depicting the change in microstructure of due to forging. In the ODS alloys, forging increased the fine grain size as compared to the HIP microstructure.

The increase in fine grain size was not as significant in Alloy 2 ODS alloys due the γ' acting as a second pinning phase preventing significant growth of the grains. In the Alloy 2 ODS forgings with higher "z" contents, some porosity remained around some of the large grain regions following forging; therefore, lower "z" contents are desired. Increasing the forging temperature led to grain growth resulting in an increase in the size and quantity of the large grain area percent which will lead to a reduction in strength due to the loss of Hall-Petch strengthening. However, the effect of the increased forging temperature was not as significant at higher dopant quantities due to an increase in the quantity of nano-oxides behaving as pinning sites and reducing the amount of grain growth. When the Alloy 2 ODS samples are forged sub-solvus the γ' size is large with the inhomogeneous banded distribution of γ' throughout the microstructure. By increasing to super-solvus forging, the γ' is significantly reduced as the primary γ' has been placed back in solution and the cooling γ' is now homogenously distributed (Figure 20).

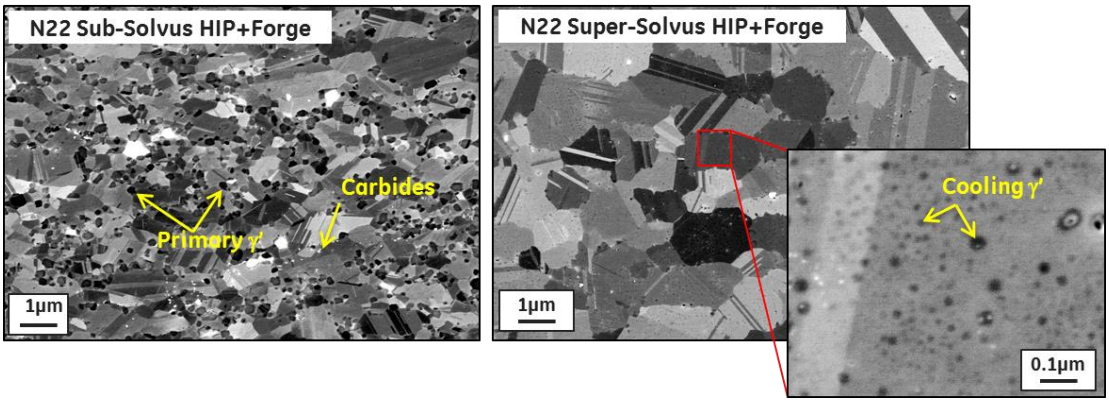

Figure 20: SEM of Alloy 2 ODS (N22) depicting the increase in grain size and decrease in γ' size due to super-solvus processing.

Following forging, the Alloy 2 baseline, Alloy 2 with 1x (N19), and Alloy 2 with 2x+1z (N21) forgings were held at three elevated temperatures T3, T6, and T8 (where T1<T3<T6<T8) for 4hr to determine the γ' solvus temperature. The post forge heat treatment led to an increase in the grain size in all cases however, the ODS samples did not coarsen as significantly as the baseline due to the additional pinning provided by the nano-oxides. The baseline PM Alloy 2 and the Alloy 2 with 2x+1z (N21) show that the γ' solvus is between T3 and T6 (Figure 21).

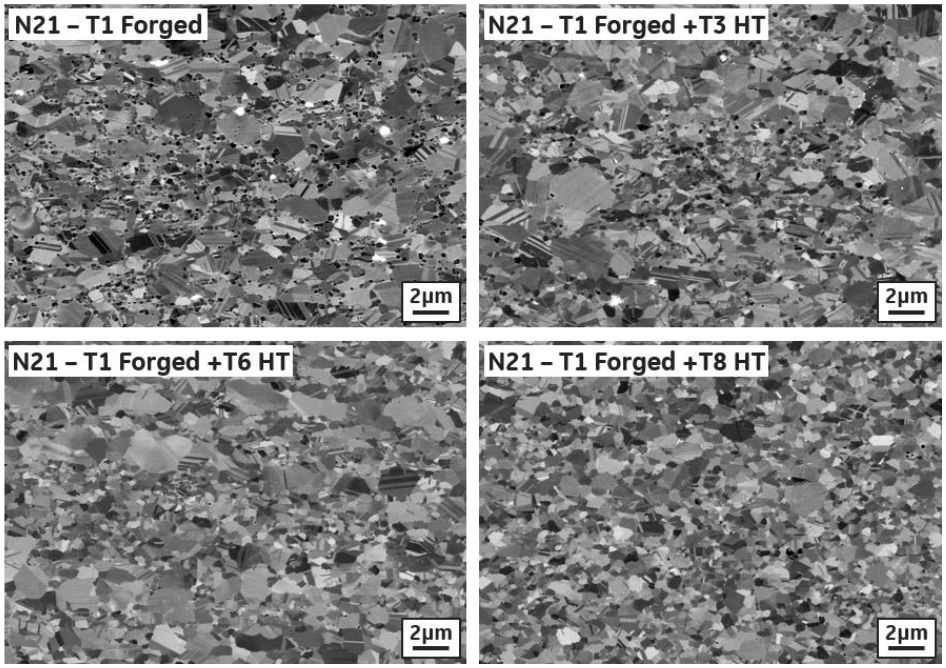

Figure 21: SEM images showing Alloy 2 powder with 2x oxide and 1z metallic dopant contents in the as-forged state and after three subsequent heat treatments (T1<T3<T6<T8). The grain size increases with increases annealing temperature and the γ' solvus was found to be between T3 and T6.

This was determined both by the significant increase in grain size as well as a direct assessment of the γ' size following cooling. This solvus result agrees with the literature value for the Alloy 2 γ' solvus. However, the Alloy 2 sample containing 1x and no "z" appears to have few to no γ' at T3.

As this alloy has no “z”, Al is stolen from the γ’ to form Al-“x” based nano-oxides which can alter the γ’ chemistry. This change in γ’ chemistry could result in a lower solvus temperature.

The TMP work detailed in the Q3 and Q4 reports showed that the nano-oxides, fine grains, coarse grains, and γ’ (when present) all undergo changes as a function of HIP temperature, forging temperature, and post-forge heat treatment. This information can be used to identify the optimal processing conditions for each alloy to yield the desired mechanical properties.

4.3 Mechanical Testing

Details of how each material was processed prior to being tested are provided in the Q4 report. Sample geometries and testing details are provided in Section 3.4.

4.3.1 Tensile Testing

The bore simulative yield strength, ultimate tensile strength, and plastic elongation to fail data for all samples tested are shown in Fig 22. The data for each composition is the result of three individual tests except for sub-scale 718, which had only two tests completed due to a machining error.

A comparison of the baseline PM Alloy 1 and PM Alloy 2 alloys shows that the γ’ precipitation strengthening of the PM Alloy 2 yields a stronger alloy as expected. Both PM alloys are approximately 20 to 25 percent stronger than their cast and wrought versions. This is likely due to the finer grain size produced via the PM processing. Despite being stronger, both PM variants maintain excellent ductility. Dispersion strengthened variations of Alloy 1 (N10 and N16) and Alloy 2 (N21) all show significant increases in yield strength and significant decreases in ductility. While ODS Alloy 1 also shows an increase in the ultimate tensile strength, the ODS version of Alloy 2 does not. For Alloy 1 ODS variants, the greater the amount of oxide added (N16 > N10), the greater the strength and lower the ductility. All ODS variants have too low a ductility to be used as a wheel material and their strengths are beyond what is required. As a result, a lower oxide loading is required to provide the necessary balance of properties.

The subscale 718 alloy produced a yield strength that was 10 percent lower than full scale material and showed an absence of delta phase precipitation on the grain boundaries. This reduction in strength is due to using a uniform aging heat treatment for the sub-scale 718 and the coprecipitation and sluggish γ’ variants rather than the conventional 718 age. A uniform aging practice was done to maintain processing uniformity. This will be discussed more in the next section. The tensile results for 718-011 and 718-027 show strengths lower than the sub-scale 718 baseline alloy. All three alloys have excellent plastic elongation to fail values. In order to match the baseline 718 tensile properties, further optimization of the 718-011 and 718-027 chemistries and/or processing is required.

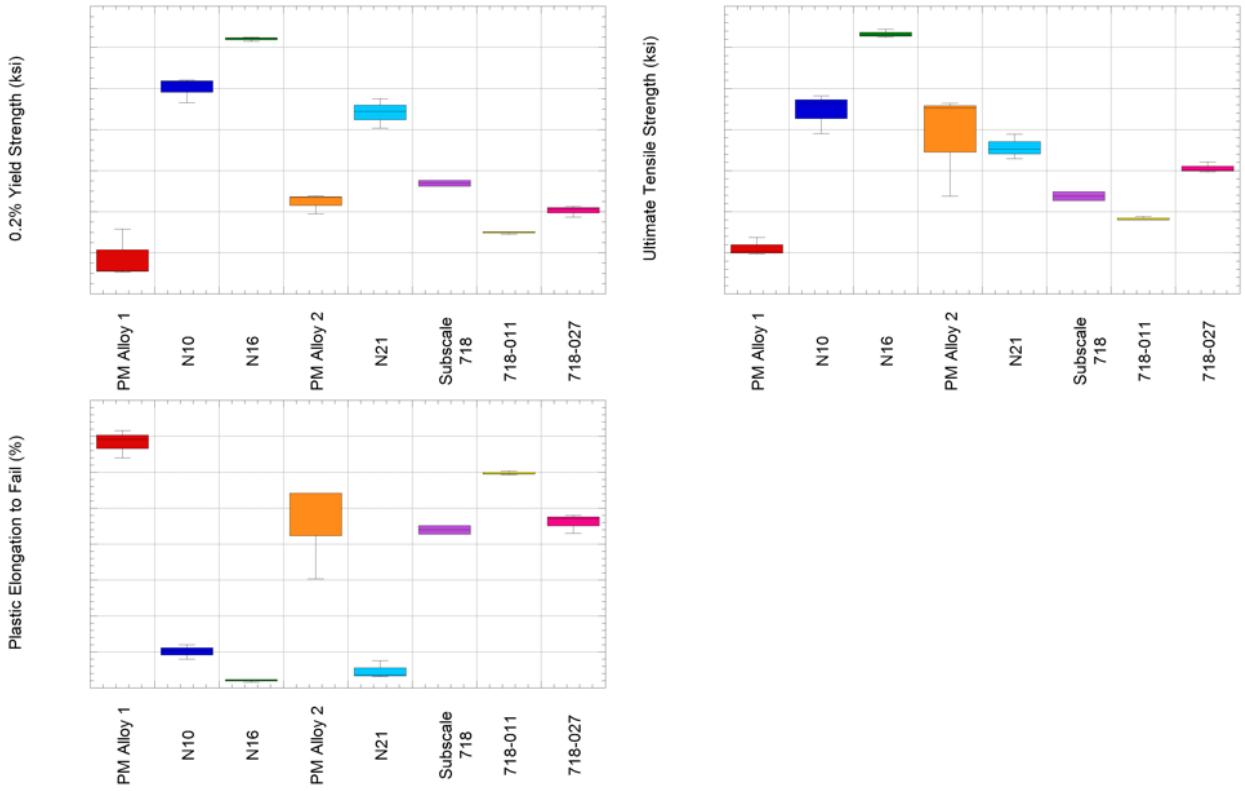

Figure 22: Bore simulative tensile results showing a) 0.2% yield strength b) ultimate tensile strength c) plastic elongation to fail.

The 718 variants were also tested at a higher temperature to understand whether they maintained their strength at rim simulative temperatures. The yield stress as a function of temperature is shown in Fig 23.

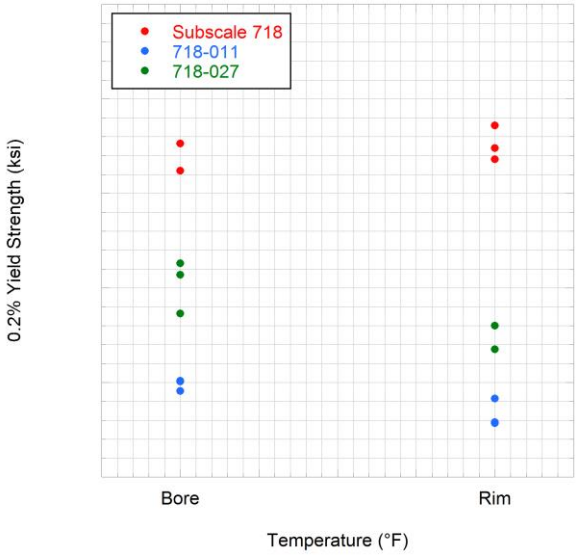

Figure 23: 0.2% yield stress as a function of temperature for the 718 variants.

The subscale 718 does not show a reduction in yield stress while the coprecipitation and sluggish gamma prime variants may show a slight decrease. Conventional Alloy 718 would be expected to show a five percent decrease in yield stress over the same temperature increase.

Because of the non-standard age utilized on the sub-scale 718, the starting yield strength was already lower than that expected at the rim simulative temperature and, as a result, no further reduction in strength was seen.

4.3.2 Hold Time Fatigue Crack Growth Testing

Fig. 24a shows the hold time fatigue crack growth data for the oxide dispersion strengthened samples. Only baseline PM Alloy 1 and PM Alloy 2 data is plotted. All ODS variants exhibited crack growth that was too fast to measure upon application of the load. Thus, their crack growth behavior is very poor. The PM Alloy 1 data shows that the crack growth rates stay relatively constant for shorter hold times and then increase at longer hold times. This change in crack growth rate indicates a change from fully cycle dependent crack growth behavior to fully time dependent crack growth behavior. The hold time at which this change occurs is called the critical period. In order to more fully define the critical period, lines of slope 0 and 1 are overlaid on the experimental data (red dashed lines in Fig. 24a). The intersection of these two lines defines the critical period. For PM Alloy 1 the critical period is approximately 900s. It is not known whether the change from fully cycle dependent to fully time dependent crack growth is driven by an environment-fatigue or a creep-fatigue mechanism. Additional testing in a vacuum could be used to separate the two mechanisms.

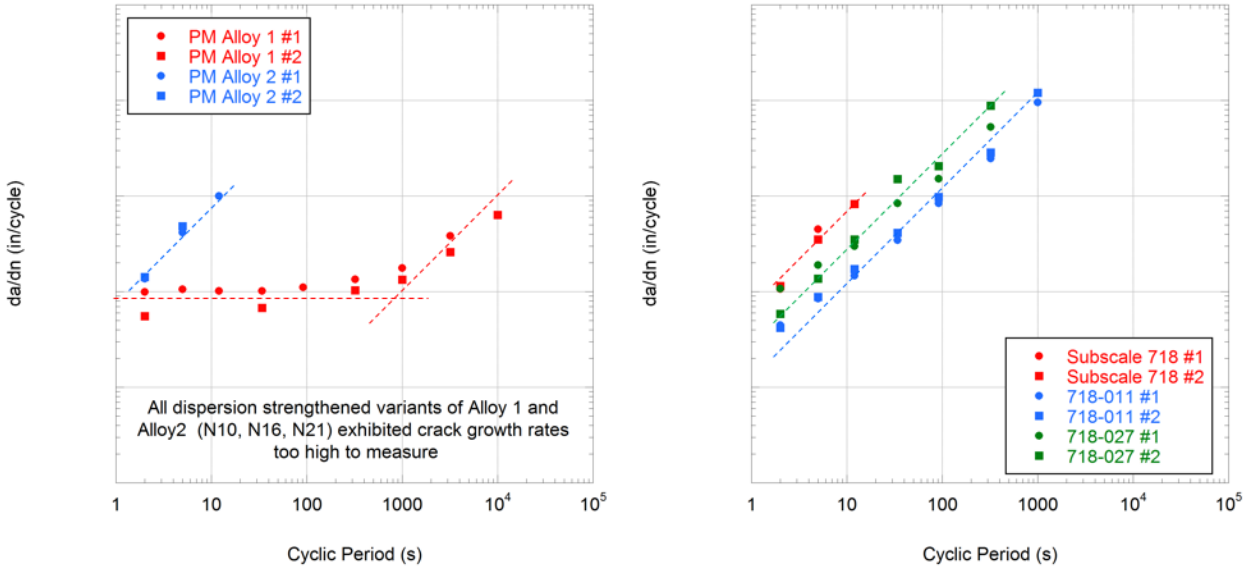

Figure 24: Hold time fatigue crack growth results for a) ODS baseline and variants and b) coprecipitation baseline and variants.

The PM Alloy 2 tests show that measurable data was only collected for cycles periods less than 12 seconds. Longer hold times result in crack growth rates that could not be measured. The two tests completed on the baseline PM Alloy 2 show that it is fully time dependent even at short hold

times. The PM Alloy 2 powder procured for this program intentionally reduced the carbon to as low a level as possible due to carbon pick-up that occurs during the milling process. This carbon pick-up during milling yields the baseline target amount of carbon for the milled powder. However, because of ordering low carbon starting material, the unmilled baseline tests completed on this program were performed on material that was not able to form the typical grain boundary carbides that aid in improving the mechanical properties of the alloy. It is thought that this is the reason that the hold time crack growth behavior is so much worse than the cast and wrought baseline data measured on a prior program which led to the choosing of this alloy. Additional characterization is required to confirm this.

Fig. 24b shows the hold time fatigue crack growth data for the subscale baseline 718 alloy and the coprecipitation/sluggish γ' samples. The coprecipitation/sluggish γ' tests show that at each hold time, their crack growths rates are lower than the baseline subscale 718. However, all alloys exhibit no cycle dependent behavior over the range of hold times tested. Rather, they exhibit fully time dependent behavior after very short hold times. Despite having lower crack growth rates, the fully time dependent behavior at short hold times needs to be significantly improved for these alloys to be viable as a wheel material.

As shown in Table 4, the subscale 718, 718-011, and 718-027 show hardness increases occurred during the hold time fatigue crack growth tests.

Sample Name	Starting Hardness (Rc)	Final Hardness (Rc)	Test Time (hr)
Subscale 718 #1	41.0	44.6	0.8
Subscale 718 #2	40.9	45.1	0.9
718-011 #1	30.6	39.1	5.2
718-011 #2	30.3	39.4	5.9
718-027 #1	35.7	39.4	2.7
718-027 #2	34.4	40.1	2.8

Table 4: Hardness results from hold time fatigue crack growth test bars.

The subscale 718 achieves its expected production hardness following test completion. It is expected that additional precipitation of γ'' causes the increase in hardness in the subscale 718. However, it is not yet known what phase(s) are driving the hardness increase in 718-011 and 718-027 and a microstructure evaluation is required. This data demonstrates that individual aging treatments are required for each alloy to ensure that full hardness is achieved prior to conducting any additional mechanical tests.

5.0 Conclusions and Recommendations

During the one year period of performance on this Phase 1 program, two fundamentally different alloying approaches have been screened to enable a heavy-duty gas turbine wheel capable of operating at 1200°F and above. Based on the experimental data produced, it was found that both methods were feasible.

The coprecipitation task demonstrated that compact coprecipitates of γ'/γ'' form during slow cooling. The chemical space of interest was assessed via experiments as well as modeling. In addition to defining a coprecipitation space of interest, this task also found a chemical window that allowed a sluggish γ' phase to form. Both types of precipitates remained fine enough following a slow cool to be useful for strengthening large heavy-duty gas turbine wheels. Following some initial thermo-mechanical processing work to define both a break down procedure and heat treat cycle, tensile and hold time fatigue crack growth properties were screened. While neither of the alloys screened met the required properties, further optimization of chemistry and thermo-mechanical processing will likely improve upon the first properties measured.

The oxide dispersion strengthening task demonstrated that a high density of nanometer-sized oxides will precipitate in both a solid solution strengthened and a γ' strengthened nickel-based superalloy. While the oxide precipitation was shown to be repeatable, the high speed milling process was prone to contamination, and the final material showed a high density of coarse brittle particles or regions where initial elemental powder additions were not fully incorporated. It is likely that these issues contributed to the poor tensile and crack growth behavior measured during property screening.

While there was no opportunity for a Phase II, this work will be continued with internal GE funds. Based on the data produced on Phase I, only the coprecipitation and sluggish γ' work will continue. This decision was reached based on two factors. First, there is no simple way forward to significantly improve the sub-scale yield of the oxide dispersion material given the energy required for milling. And second, the mechanical properties of the coprecipitation alloys are closer to meeting the required properties. Furthermore, if successful on the lab scale, full scale production infrastructure is already in place to allow rapid scale up of the coprecipitation material.